

Tidal currents on the central Oregon shelf: Models, data, and assimilation

Svetlana Y. Erofeeva, Gary D. Egbert, and P. M. Kosro

College of Oceanic and Atmospheric Sciences, Oregon State University, Corvallis, Oregon, USA

Received 28 August 2002; revised 13 January 2003; accepted 19 February 2003; published 17 May 2003.

[1] Measurements of tidal currents on the central Oregon shelf are available from several sources, including recent high frequency (HF) coastal radar and Acoustic Doppler Profiler (ADP) deployments, and historical current moorings. In this paper we use a generalized inverse (GI) approach to compare these data to, and then assimilate them into, numerical models for the barotropic tides. Harmonic analysis of the data in short time windows using a modified admittance approach reveals that tidal currents on the Oregon shelf are highly variable in time, and can contain significant baroclinic components. Data from the winter months, when waters on the shelf are only weakly stratified, are found to be most nearly barotropic and thus most reasonable for assimilation into the shallow water equations model. The various data sources are used in several different combinations for assimilation and validation. Forcing the prior forward model with normal flow open boundary conditions obtained from a regional barotropic inverse model results in semidiurnal barotropic currents that are consistent (within estimated error limits) with all available data. In contrast, diurnal currents on the shelf are very sensitive to details of the model configuration, and are significantly improved by data assimilation. Very similar solutions result from assimilation of either the HF radar or ADP data sets. The high sensitivity of the diurnal band currents can be understood dynamically in terms of trapped shelf waves. A short (~ 85 km long) section of shelf off the central Oregon coast is wide enough to allow first-mode barotropic shelf waves at the subinertial diurnal frequencies. This results in locally resonant large amplitude diurnal tidal currents that are very sensitive to details in the local forcing, and hence quite variable in time.

INDEX TERMS: 1255 Geodesy and Gravity: Tides—ocean (4560); 4560 Oceanography: Physical: Surface waves and tides (1255); 3210 Mathematical Geophysics: Modeling; 3260 Mathematical Geophysics: Inverse theory; *KEYWORDS:* tides, tidal currents, data assimilation, inverse modeling

Citation: Erofeeva, S. Y., G. D. Egbert, and P. M. Kosro, Tidal currents on the central Oregon shelf: Models, data, and assimilation, *J. Geophys. Res.*, 108(C5), 3148, doi:10.1029/2002JC001615, 2003.

1. Introduction

[2] With the availability of modern satellite altimeter data, tidal elevations in the open ocean can now be mapped empirically over most of the global ocean with an accuracy approaching 1 cm [e.g., Shum *et al.*, 1997; Le Provost, 2001]. The highly accurate altimeter data, together with the shallow water equations, can also be used to infer barotropic tidal currents [e.g., Egbert *et al.*, 1994; Ray, 2001; Egbert and Ray, 2001], with accuracies approaching 5–10% in the open ocean [Dushaw *et al.*, 1997]. In coastal and shallow seas, where tidal wavelengths are shorter and topographic complications are generally more severe, our knowledge of the tides is much poorer. Given the short spatial scales and the relative paucity of observations, direct empirical mapping of tidal fields in these areas is seldom possible. Accurate modeling is also a challenge, especially with regard to currents, which are highly sensitive to topographic

variations, specification of open boundary conditions, and parameterizations of dissipative processes [e.g., Lefevre *et al.*, 2000]. While our knowledge of tides in the coastal ocean is comparatively poor, tidal currents in shallow water are often strongly amplified, and thus of relatively greater importance. Even in a narrow shelf environment such as off the Oregon coast a significant fraction (20–50%) of the total kinetic energy is found in the diurnal and semidiurnal bands [Torgimson and Hickey, 1979]. In areas with broad shelves (e.g., the European shelf) tidal currents can dominate the spectrum. These strong currents have important implications for practical maritime applications, as well as more general physical and biological processes in the coastal ocean [e.g., Prandle, 1997]. Accurate modeling of tidal currents is thus an important part of the coastal ocean prediction problem.

[3] Data assimilation methods allow one to optimally combine diverse data with dynamical equations, and thus provide the most promising approach to accurate mapping of tidal current fields in the coastal environment. A formal generalized inverse (GI) approach [e.g., Bennett, 1992;

Egbert et al., 1994], also provides a rational framework for qualitative comparison between data and a numerical model. Hypotheses concerning the representativeness of data or the accuracy of a model can be formally tested. In this paper we assume shallow water dynamics and apply the GI method to study barotropic tidal currents in the coastal ocean off central Oregon. Efforts to extend this work to modeling of internal tides on the central Oregon shelf are described by *Kurapov et al.* [2003].

[4] We have four goals in this study: (1) to provide an example application of the GI method to assimilation of tidal current data; (2) to quantitatively compare tidal current data from several distinct sources, and from models; (3) to map tidal currents on the central Oregon shelf; and (4) to better understand tidal dynamics in this area. The model configuration and inversion approach are outlined briefly in section 2, and initial forward modeling results are presented in section 3. The data, including HF radar measurements of surface currents [*Kosro et al.*, 2000], an ADP mooring and historical current meters, are described and analyzed in section 4. These data show that tidal band currents on the Oregon shelf can be highly variable in time, and can contain significant baroclinic components. Given that we assume shallow water dynamics, and that most of the data sources do not sample the full water column, our first challenge is to extract barotropic tidal “harmonic constants” that can be realistically represented by the model, along with error bars. Our general approach is to first analyze the data in short time windows, and then select times when currents are most nearly barotropic. In general only data from the winter months, when waters on the shelf are more weakly stratified, are reasonably consistent with our simplified dynamics.

[5] In section 5 we use the estimated harmonic constants to refine our model of barotropic shelf currents, and to assess consistency between model and data, and our a priori estimates of error levels. The various data sources are used in several different combinations for assimilation and validation. We find that, provided open boundary conditions are of sufficient quality, semidiurnal currents from the forward model are already consistent (within the estimated error bars) with the observations. In contrast, diurnal currents on the shelf are very sensitive to details of the model configuration, and are significantly improved by assimilation of data. The dynamical significance of these results is considered in section 6, where we show that in a short (~ 85 km) section off the central Oregon coast the shelf becomes wide enough to allow first-mode barotropic coastally-trapped waves at the subinertial diurnal frequencies. This may result in locally resonant large amplitude tidal currents that are very sensitive to errors in boundary conditions or the simplified dynamical equations.

2. Modeling and Assimilation

2.1. Model Domain

[6] To model tides on the Oregon shelf we use a one way nesting approach, with open boundary conditions for each domain determined from a coarser resolution inverse solution. The local model domain has a resolution of 1 km with longitude and latitude limits 234°E – 236°E , 43°N – 45.7°N , (185×300 km), covering most of the Oregon

Coast (Figure 1b). Bathymetry was derived from NOAA SeaBeam and BSSS swath bathymetry presented by *Goldfinger et al.* [2000]. The local domain is nested within a regional scale $1/12^\circ$ degree ($\sim 1335 \times 1564$ km) domain which extends from 224°E to 240°E and from 36°N to 50°N . The ETOPO-5 database (National Geophysical Data Center, 1992) was used to define bathymetry for this domain, which includes the coasts of Southern British Columbia, Washington, Oregon and Northern and Central California (Figure 1a). The regional model assimilated TOPEX/POSEIDON altimeter data, with boundary conditions obtained from TPXO.5, a $1/2^\circ$ nearly global inverse solution derived as by *Egbert et al.* [1994] and *Egbert* [1997]. The extra step of constructing an intermediate scale inverse model was taken to provide improved resolution of prior boundary conditions for the local domain. In the global model the entire local domain is only about four grid cells wide, and the narrow Oregon shelf is not resolved.

[7] At regional scale the topography off central Oregon is relatively simple, with a nearly straight coast, and a narrow continental shelf defined by nearly parallel bathymetric contours (Figure 1a). The higher resolution bathymetry (Figure 1b) reveals details that deviate considerably from this simple picture. Near 44°N the shelf abruptly widens, with the 200-m depth contour jumping 20–30 km to the west. This broader region of the shelf contains two shallow banks, Heceta Bank (44°N , 235.9°E) and Stonewall Bank (44.55°N , 235.65°E). We refer to this widened area of shelf as the Heceta-Stonewall Bank Complex (HSBC). West of the HSBC the shelf ends abruptly, with depths increasing to over 1000 m in less than 10 km, and 2000 m in about 20 km. South, and especially north, of this area topography is simpler, the shelf is narrower, and slopes are more gradual.

2.2. Dynamics

[8] We assume shallow water dynamics,

$$\frac{\partial \mathbf{U}}{\partial t} + f \hat{\mathbf{z}} \times \mathbf{U} + \mathbf{F} + \mathbf{U} \cdot H \nabla \mathbf{U} + A_H \nabla^2 \mathbf{U} = \mathbf{f}_0 + g \cdot H \nabla (\zeta - \zeta_{SAL}) \quad (1)$$

$$\frac{\partial \zeta}{\partial t} = -\nabla \cdot \mathbf{U},$$

where ζ is the elevation of the sea surface; \mathbf{U} is the volume transport vector, equal to velocity times water depth H , f is the Coriolis parameter, $\hat{\mathbf{z}}$ is oriented to the local vertical. Dissipative terms include the standard quadratic parameterization of bottom friction $\mathbf{F} = (c_D \|\mathbf{v}\|/H) \mathbf{U}$ (with $c_D = 0.0025$), and horizontal viscosity with constant eddy coefficient $A_H = 10^2 \text{ m}^2 \text{ s}^{-1}$. The astronomical tide generating force, with allowance for Earth’s body tide [*Hendershott*, 1977], is denoted by \mathbf{f}_0 . Tidal loading and self-attraction [*Hendershott*, 1972; *Ray*, 1999] are accounted for by the term ζ_{SAL} , which is taken as a fixed forcing, computed by convolution of the global tidal solution TPXO.5 with the appropriate Greens functions, as described by *Ray* [1999].

[9] Boundary conditions for equation (1) are no flow across (and no-slip along) the coast, and specification of either elevations or the normal component of volume transports on (and free slip along) any open boundaries. The system of equation (1) is discretized on a C-grid, and solved

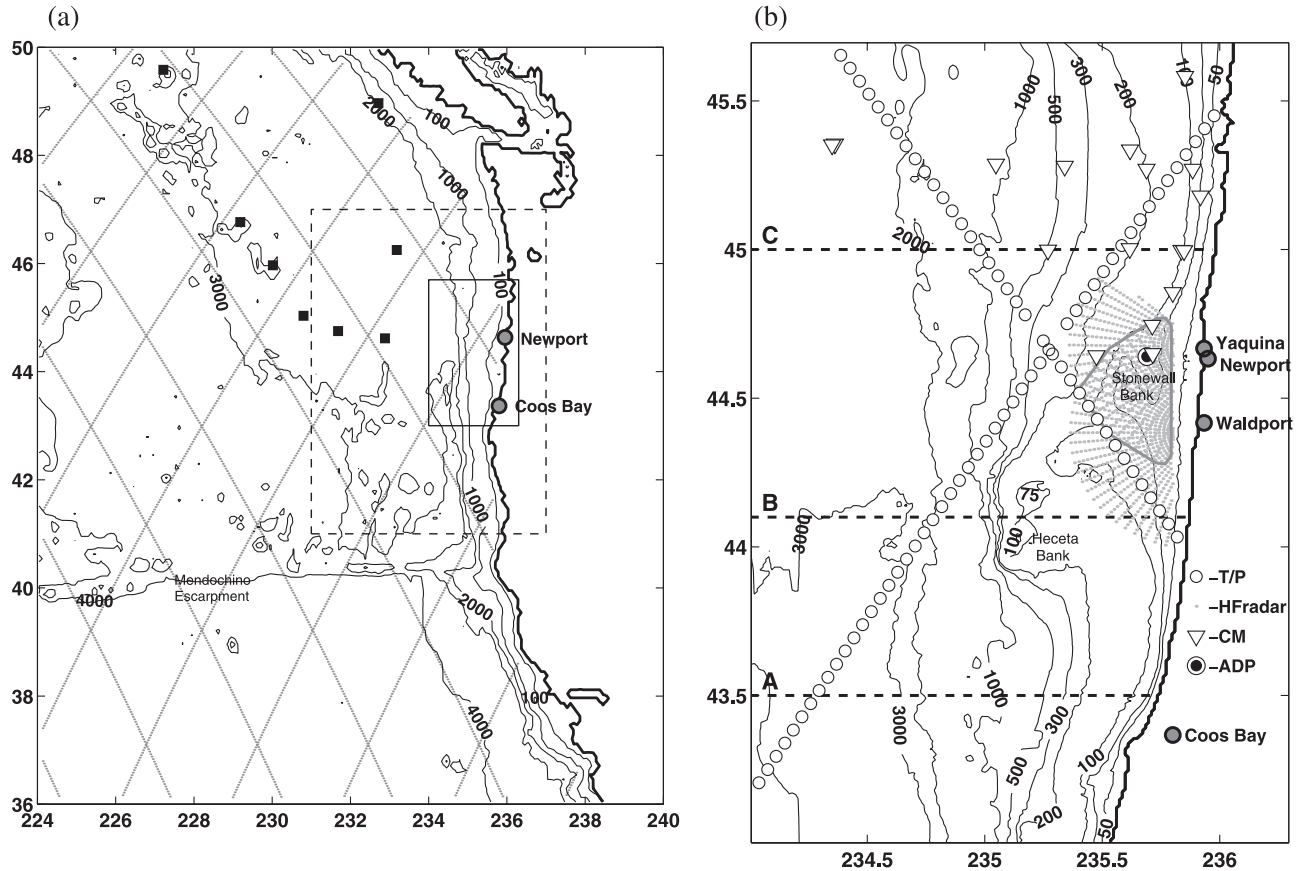


Figure 1. (a) Regional and (b) local model domains with data locations. Bathymetry contours are in meters. The local domain is outlined by the inner box in Figure 1a. Satellite ground tracks are shown with dots in Figure 1a and with circles in Figure 1b. Pelagic tide gauges are denoted by solid squares in Figure 1a. HF radar bins are shown with dots in Figure 1b, with the area of HF radar overlap outlined. Historic current meter moorings are denoted by triangles, and the ADP location by a double circle.

either by time stepping with a periodic forcing followed by harmonic analysis [e.g., Egbert *et al.*, 1994], or in the frequency domain by directly factoring the coefficient matrix for a linearized version of the system [Egbert and Erofeeva, 2002] (hereinafter referred to as E&E). In the latter case the quadratic friction is linearized and the advective and lateral viscosity terms are omitted. The simpler (and much faster) linearized approach is used primarily for the inverse calculations; see E&E for further details.

2.3. Inverse Methods

[10] Egbert *et al.* [1994], Egbert and Bennett [1996], Egbert [1997], and E&E provide a detailed description of a generalized inverse (GI) scheme for incorporating observational data into barotropic tidal models. Here the GI scheme is used to improve the accuracy of the regional and local solutions by assimilating TOPEX/Poseidon altimetry data, and to synthesize and compare local scale models and observations of tidal currents on the Oregon shelf. With the GI approach we compromise between satisfying the hydrodynamic equations (1) and fitting the observations by minimizing the quadratic penalty functional,

$$J[\mathbf{d}, \mathbf{u}] = (\mathbf{L}\mathbf{u} - \mathbf{d})^\dagger \Sigma_d^{-1} (\mathbf{L}\mathbf{u} - \mathbf{d}) + (\mathbf{S}\mathbf{u} - \mathbf{f}_0)^\dagger \Sigma_f^{-1} (\mathbf{S}\mathbf{u} - \mathbf{f}_0). \quad (2)$$

Here \mathbf{u} represents the tidal fields U and ζ , $\mathbf{S}\mathbf{u} = \mathbf{f}_0$ is shorthand for the system of equations (1), $\mathbf{L}\mathbf{u} = \mathbf{d}$ relates the observations to the unknown tidal state \mathbf{u} , and Σ_d , Σ_f are covariances for the data and dynamical errors. These covariances express our a priori beliefs about the magnitude and correlation structure of errors in the data, and in the assumed dynamical equations.

[11] To the extent that these covariances are defined in a rational way, the GI solution combines data and dynamics in an optimal fashion, and provides a posteriori estimates of errors in the inverse solution. Perhaps more importantly, as a statement of a priori belief the covariances represent a testable hypothesis, about both the adequacy of the ocean model and the quality and representativeness of the data [e.g., Bennett, 1992; Chua and Bennett, 2001]. GI thus provides a natural framework for quantitative comparison of numerical models and data.

[12] For the dynamical error covariance Σ_f we retain the general form discussed by Egbert *et al.* [1994] with no correlation between errors in the dynamical equations and errors in the boundary conditions. As discussed by Bogden [2001] this assumption may not be reasonable, especially for a very small local domain. Future efforts to relax this restriction, especially in the context of nested data assimilation, are certainly warranted. For the errors in the dynamical

ical equations, we allow for spatially varying amplitudes, with a constant decorrelation length scale of 5 km. A range of larger decorrelation length scales was tested, and the assimilation was found to perform slightly better in this shallow domain with shorter decorrelation scales. This is consistent with our assumption that errors are dominantly in bathymetry and dissipation. Error variances were estimated as a function of position in the model domain following the analysis of *Egbert et al.* [1994], using the prior (or first guess) tidal model to estimate typical values of the tidal fields. For the local domain the two dominant sources of error in the equations are due to errors in the bathymetry (assumed to be 2%), and errors in the parameterization of dissipation (50% of the amplitude of the appropriate terms in the prior). For the regional scale and global models, larger errors are assumed (5% and 100%, for bathymetry and dissipation, respectively [*Egbert et al.*, 1994]).

[13] To define error covariances for open boundary conditions we again adopt a nesting approach, with the posterior error covariance for the regional inverse solution used as the prior covariance for the local model. Posterior error covariances were calculated with a Monte Carlo approach, as described in E&E. For data errors we assume a diagonal covariance. Details of error variance estimates for each data type are discussed below in the data processing section. The representer approach [*Bennett*, 1992], with modifications described by *Egbert et al.* [1994] and E&E is used to minimize equation (2).

3. Modeling Results

3.1. Regional Model

[14] For the regional model 232 orbit cycles of TOPEX/POSEIDON altimeter data were assimilated using the inverse methods outlined above. Eight pelagic tide gauges [*International Association for Physical Sciences of the Oceans*, 1992] were used for validation. The satellite ground tracks and tide gauge locations are shown in Figure 1a. The prior solution for the regional inverse model was obtained by solving equation (1) by time stepping with normal flow boundary conditions taken from the global inverse solution TPXO.5. The inverse solution improves fit to the validation tide gauges compared to the prior only insignificantly. For example, for M_2 RMS misfits are reduced from 1.11 to 1.10 cm and for K_1 from 1.52 to 1.50 cm. Evidently the altimeter data, which have already been used to constrain the global model (and hence the open boundary conditions for the prior) contain little additional information about tidal elevations.

[15] Elevations and currents for the principal semidiurnal and diurnal constituents M_2 and K_1 are shown for the central portion of the domain (outlined with the dotted line in Figure 1a) in Figure 2. Currents are plotted as vectors separately for in-phase and quadrature components. Here, and subsequently, in-phase refers to the standard Greenwich phase; that is, the in-phase plots give the tidal currents when the phase of the tidal potential is zero at the Greenwich meridian. The quadrature component gives the current 1/4 of a tidal period earlier.

[16] As is well known from many previous studies on the West Coast of North America both semidiurnal and diurnal constituents have a dominantly Kelvin wave character with

phase propagation to the North, and currents in deep water aligned parallel to the coast [e.g., *Munk et al.*, 1970; *Crawford and Thomson*, 1984; *Rosenfeld and Beardsley*, 1987; *Flather*, 1987]. Off Oregon, alongshore currents lag high water (by approximately 45° for M_2 , 10° for K_1). For a pure Kelvin wave over a flat bottom, currents are in phase with elevations, so this simple picture does not provide a complete description of the tides in the area. *Munk et al.* [1970] modeled tides off Southern California as a sum of a locally forced response, a Kelvin wave and Poincare type modes for a straight coast with a simple shelf. A simplified version of this model, that ignores the narrow Oregon shelf, was fit to the regional model elevations and currents. This simple model reproduces the general pattern for both constituents. For M_2 the ratio of Kelvin wave to Poincare mode amplitudes is 9:4 and the forced response is negligible. For the subinertial K_1 frequency, no Poincare type modes are allowed [e.g., *Munk et al.*, 1970], and the forced response was more significant (15% of the dominant Kelvin wave component).

[17] For a Kelvin wave along a perfectly straight coast with no alongshore topographic variations, cross-shore currents would be essentially restricted to the shelf, and would lag high water by 90° [e.g., *Munk et al.*, 1970]. For the semidiurnal (superinertial) constituent M_2 this general pattern can be discerned (with some complications due to alongshore variations in shelf topography, and probably also the Poincare modes). For the subinertial constituent K_1 , currents on the shelf are more complex, with localized areas where currents reverse directions and phases vary rapidly. These short wavelength variations are suggestive of topographically trapped shelf waves, which have frequently been observed in diurnal tidal currents at high latitudes [e.g., *Cartwright*, 1969; *Dai-fuku and Beardsley*, 1983; *Crawford and Thomson*, 1982]. However, the regional model, with a resolution of 10 km, barely resolves the shelf, and certainly does not adequately resolve slopes or alongshore topographic variations well enough to accurately model shelf wave currents..

3.2. Local Prior Model

[18] Using normal flow boundary conditions obtained from the West Coast regional model of Figure 2, we solved the system (equation (1)) for the local domain of Figure 1b, again by time stepping. This provides the prior solution for our experiments with assimilation of local observations of tidal currents.

[19] Tidal elevations in the local prior solution have large scale, and are for the most part indiscernible from the regional model results plotted in Figure 2. However, the higher resolution local model refines the map of tidal currents considerably (Figure 3). In contrast to the regional solution the tidal velocity fields are now reasonably smooth right up to the coast. The broadening of the shelf and the very steep slope near Heceta Bank have a noticeable effect on both M_2 and K_1 , locally intensifying currents on the shelf for both constituents. However, there are differences in the character of the diurnal and semidiurnal current fields, particularly over the HSBC, where the K_1 currents become very complex. Forward modeling experiments using variations in the friction parameterization, boundary conditions, and domain size show that diurnal currents in this area are very sensitive to details in the model configuration. Much

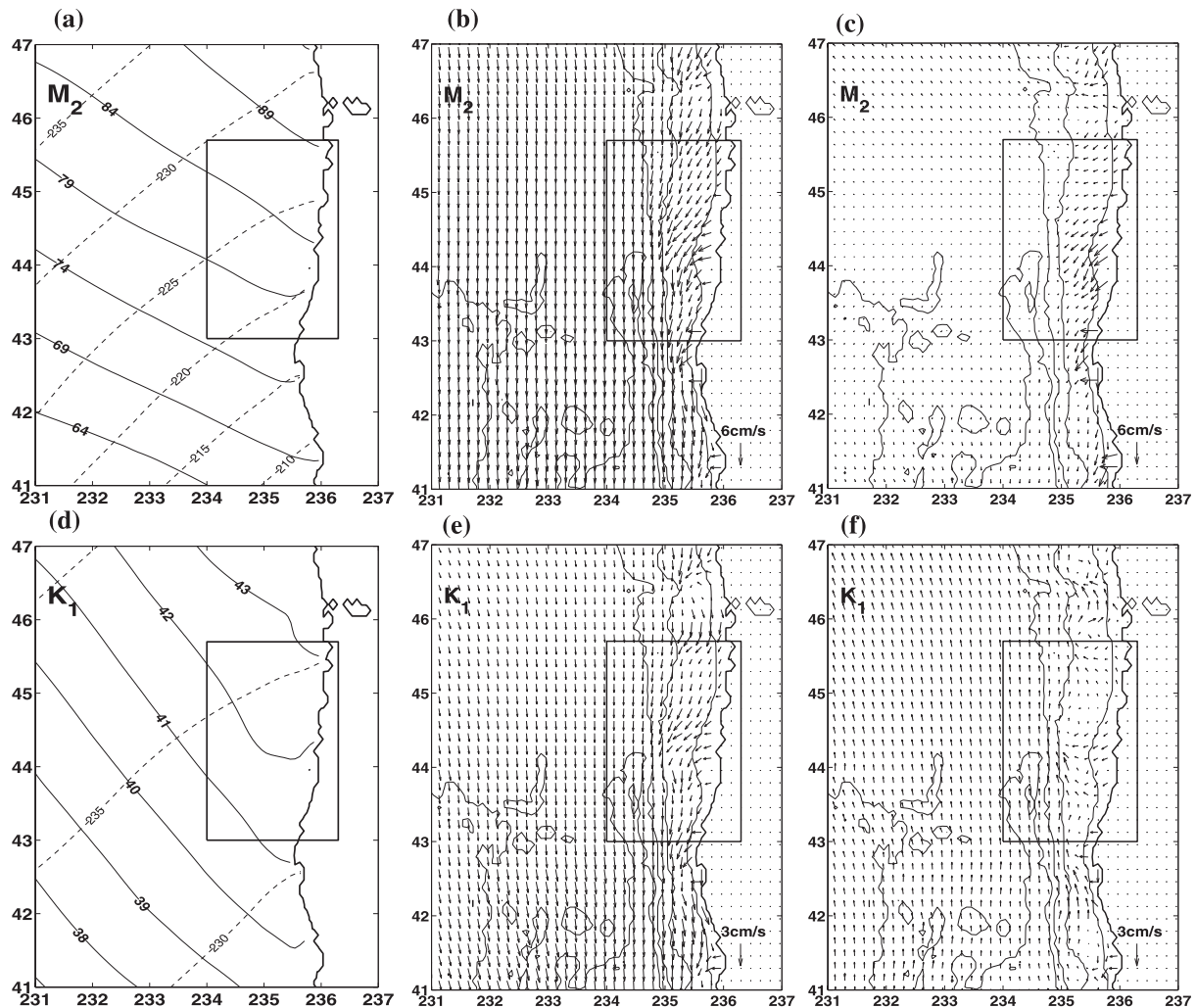


Figure 2. M_2 and K_1 elevation and currents for the regional model. Only the central portion of the regional domain, outlined with the dotted line in Figure 1a is shown. The local domain is outlined with a solid line. (a, d) Dashed lines contour Greenwich phase (in degrees increasing in the direction of propagation), and solid lines give amplitude in centimeters. (b, e) In-phase (with the gravitational potential at Greenwich) currents; (c, f) Quadrature currents, 1/4 tidal period earlier. Short wavelength variations on currents near the coast, suggestive of shelf waves, are observed in Figures 2e and 2f around the HSBC and Astoria fan. Current vector magnitudes are trimmed to 6 cm/s for M_2 and to 3 cm/s for K_1 .

larger currents (~ 6 cm/s), which vary rapidly and even reverse direction over the HSBC, are generated for some cases. We consider this behavior and its dynamical significance in more detail below.

4. Data Analysis

[20] Three different types of velocity data were used for comparison to, and assimilation into, the local barotropic model. The data from sites shown in Figure 1b include the following:

[21] • Historic current meter data were from 17 moorings from the CUE-1 (April–October 1972 [Pillsbury *et al.*, 1974a]); CUE-2 (June–September 1973 [Pillsbury *et al.*, 1974b]); SUCS (August–October 1977/1978) and WISP, (January–September 1975 [Gilbert *et al.*, 1976]) experiments. Each mooring generally included three current meters distributed through the water column.

[22] • Surface currents were derived from HF radar data (November 1997 to June 1998). The HF measurements were made from a pair of SeaSonde instrument systems, manufactured by CODAR Ocean Sensors, located at 44.67°N , 235.92°E and 44.38°N , 235.91°E , designated YHS1 and WLD1 and operated at 12.1 and 13.4 MHz, respectively. Cross-spectral data were processed to radial vectors every 10 min, which were then averaged over 1 hour [Lipa and Barrick, 1983]. The systems were operated with a bandwidth of 75 kHz, providing cells 2 km in width radially; cells were 5° wide azimuthally. Where data from two systems overlap (i.e., within the domain outlined with gray line in Figure 1b) the currents may be resolved into u and v components.

[23] • One ADP mooring was deployed within the HF radar area, at $44^\circ39'\text{N}$, $235^\circ42'\text{W}$, with a bottom depth of 80 m. Data used here were collected from 12 m to 68 m, in a time period that overlapped (but does not exactly

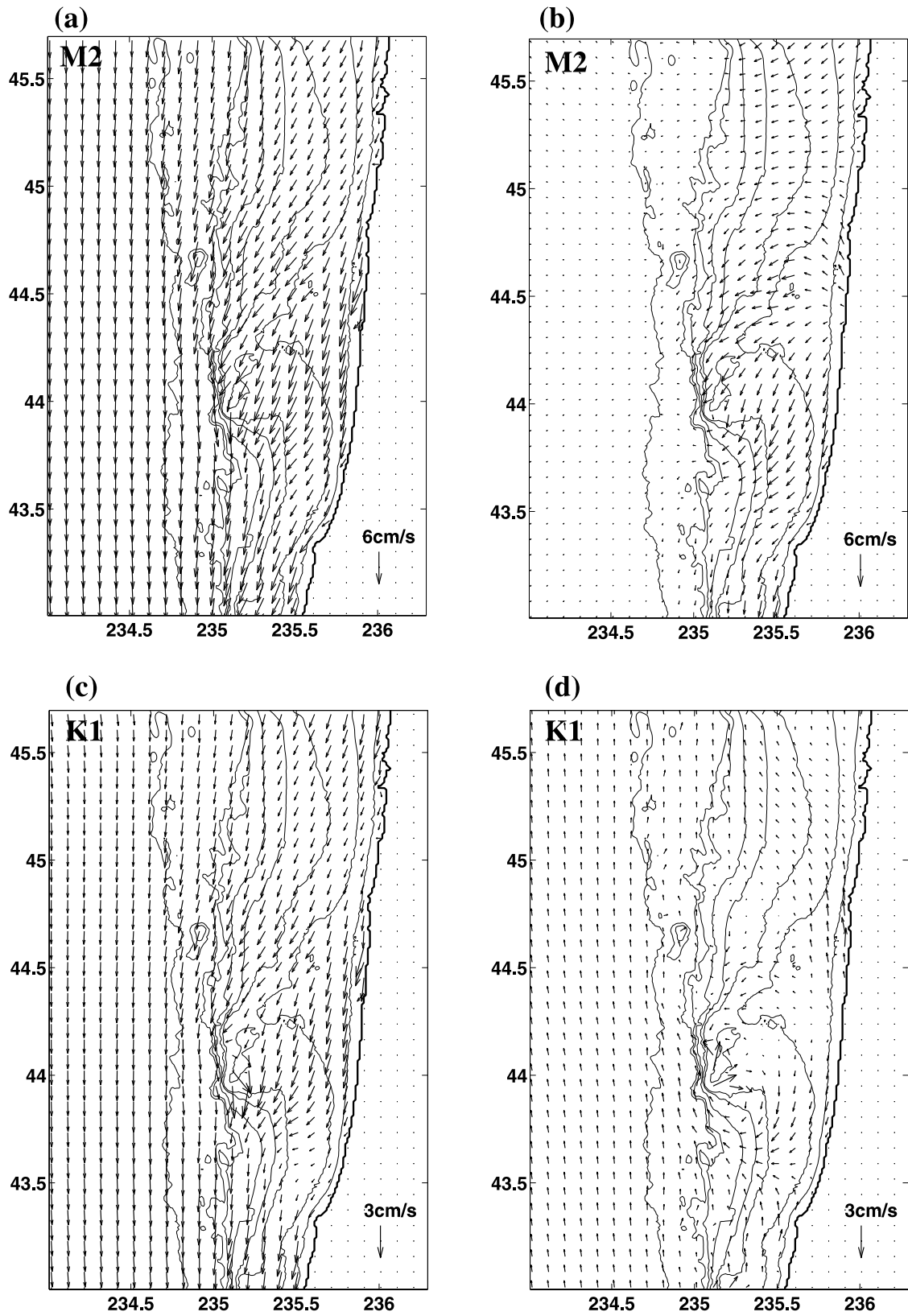


Figure 3. Local prior model M₂ and K₁ in-phase and quadrature currents, as defined in Figure 2 caption.

coincide with) dates for which HF radar data are available. Currents used for our analysis were sampled once per hour in 15 vertical bins spaced 4 m apart.

4.1. Data Analysis Approach

[24] All of these data sets require harmonic analysis prior to assimilation into the frequency domain model. Furthermore, as we can represent only the depth-averaged currents in our barotropic model, any baroclinic signals must be treated as data errors. This is of course a very serious issue for the HF radar data, which samples only the surface currents. It is also a potentially significant problem for all of the historical current moorings. Only the ADP samples enough of the water column to allow a straightforward estimate of depth-averaged currents. To better understand possible baroclinic tidal signals and non-tidal but quasiperiodic oceanographic signals, such as diurnal wind-forced oscillations, we began our processing with an exploratory analysis that allowed us to resolve temporal variations in tidal band signals.

[25] Time series were high-pass filtered (with a long-period cutoff of 48 hours) and divided into short segments (2 weeks for the results reported here, but we tried both shorter and longer windows). An admittance approach similar to that of *Zelter and Munk* [1975] was then used to estimate diurnal and semidiurnal harmonic constants for each short time window. The admittance approach is based on the hypothesis that the local response to tidal forcing varies smoothly with frequency. For example, if $v_l(\mathbf{x})$ is the harmonic constant of alongshore velocity for constituent l at frequency ω_l and location \mathbf{x} , and r_l is the complex forcing (amplitude and phase) for this constituent, the admittance $a(\mathbf{x};\omega_l) = v_l(\mathbf{x})/r_l$ is assumed to be a smooth function of ω within a tidal band. By representing the frequency dependence of the admittance $a(\mathbf{x};\omega)$ in terms of a small number of basis functions a large number of tidal constituents can be accounted for with a small number of free parameters. This allows approximate resolution of nearby constituents with even a short time series. In the most common application, three to four basis functions are used for each tidal band, to allow separation of constituents such as P_1 and K_1 with only a few months of data. In our application, we use very short time windows, and hence have very limited frequency resolution, so we take the admittance to be a constant for each of the semidiurnal and diurnal bands. Thus, for the semidiurnal band, we assume for the alongshore velocity harmonic constants at data location \mathbf{x}

$$v_l(\mathbf{x}) \approx a_{SD}(\mathbf{x})r_l, \quad (3)$$

where r_l , $l = 1, n_c$ are the forcing (or reference) complex harmonic constants for the semidiurnal constituents. These reference constants carry information about the relative amplitude and phase (for each constituent) of the open ocean tidal fields that force the local response. Here we used harmonic constants of depth-averaged alongshore velocity from the ADP mooring for the reference harmonic constants r_l , and then estimated the admittance parameters a_{SD} , a_D for each data location by least squares fitting of the time series in each window. Experiments with other reference harmonic constants (e.g., alongshore velocities off the coast of Oregon from the global inverse solution) yielded similar results.

[26] Using these estimates in equation (3), we can then compute time sequences (for all locations in the HF radar array, or depths for the current moorings) of harmonic constants for the dominant constituents in each band: M_2 for the semidiurnal band and K_1 for the diurnal. Plots of these, along with a complex empirical orthogonal functions (EOF) analysis of the sequence of harmonic constants, provide insight into temporal variations in the pattern of tidal currents. Of course our assumption of constant impedance within each band can be only approximately valid, especially when very short spatial scale internal tides are present. At least some of the temporal variability in the harmonic constant estimates results from violation of this simplifying assumption. However, the simplified admittance approach proved useful for a qualitative preliminary analysis. Based on the lessons learned from this analysis, time windows were selected when currents were most barotropic, and a more conventional harmonic analysis approach was used to estimate barotropic tidal constants for assimilation into the local model. The admittance results were also used to help estimate data error levels, another critical input to the assimilation experiments.

4.2. ADP Data

[27] The ADP mooring data provide direct information about the depth dependence of tidal currents and their seasonal variations, and thus provide a very important calibration for our analysis of the HF radar data. The data cover parts of two years, from August 1997 to February 1999. There is one significant gap due to instrument failure, between January and April 1998.

[28] We used the admittance approach outlined above with a two week sliding window to estimate time varying harmonic constants for the M_2 and K_1 constituents. Results for depth-averaged currents for M_2 , and for (baroclinic) deviations from these averages, are plotted as tidal ellipses in Figure 4a. The first three EOFs for the baroclinic variations (scaled by the corresponding mode amplitude) are plotted to the right in Figure 4b. The depth-averaged semidiurnal currents at the ADP site (top of Figure 4a) are aligned primarily alongshore and rotate clockwise. Note that in Figure 4 and subsequently, tidal ellipses with clockwise rotations are shaded with gray. The polarization ellipses are fairly stable throughout the measurement period. In contrast, there are significant temporal variations in the profiles of baroclinic ellipses which generally rotate counter-clockwise (lower part of Figure 4a). Note that shorter timescale variations, in particular those associated with the fortnightly spring-neap cycle, will be filtered out by our processing approach. These internal tides are strongly dominated by low modes, with a clear seasonal variation in amplitude, and somewhat variable phase. As indicated by Figure 4b the dominant EOFs are at least qualitatively similar to the first few flat-bottom dynamical modes. For plotting the EOF modes are scaled with the corresponding mode amplitudes (resulting from the EOF analysis) to show their relative power. Amplitudes are greatest during the summer and early fall, when the baroclinic component often exceeds the depth average by a factor of 2 or so. Allowing for spring-neap modulations and other more rapid variations peak baroclinic velocities in the tidal band could be considerably larger. These results are consistent with the observations of *Tor-*

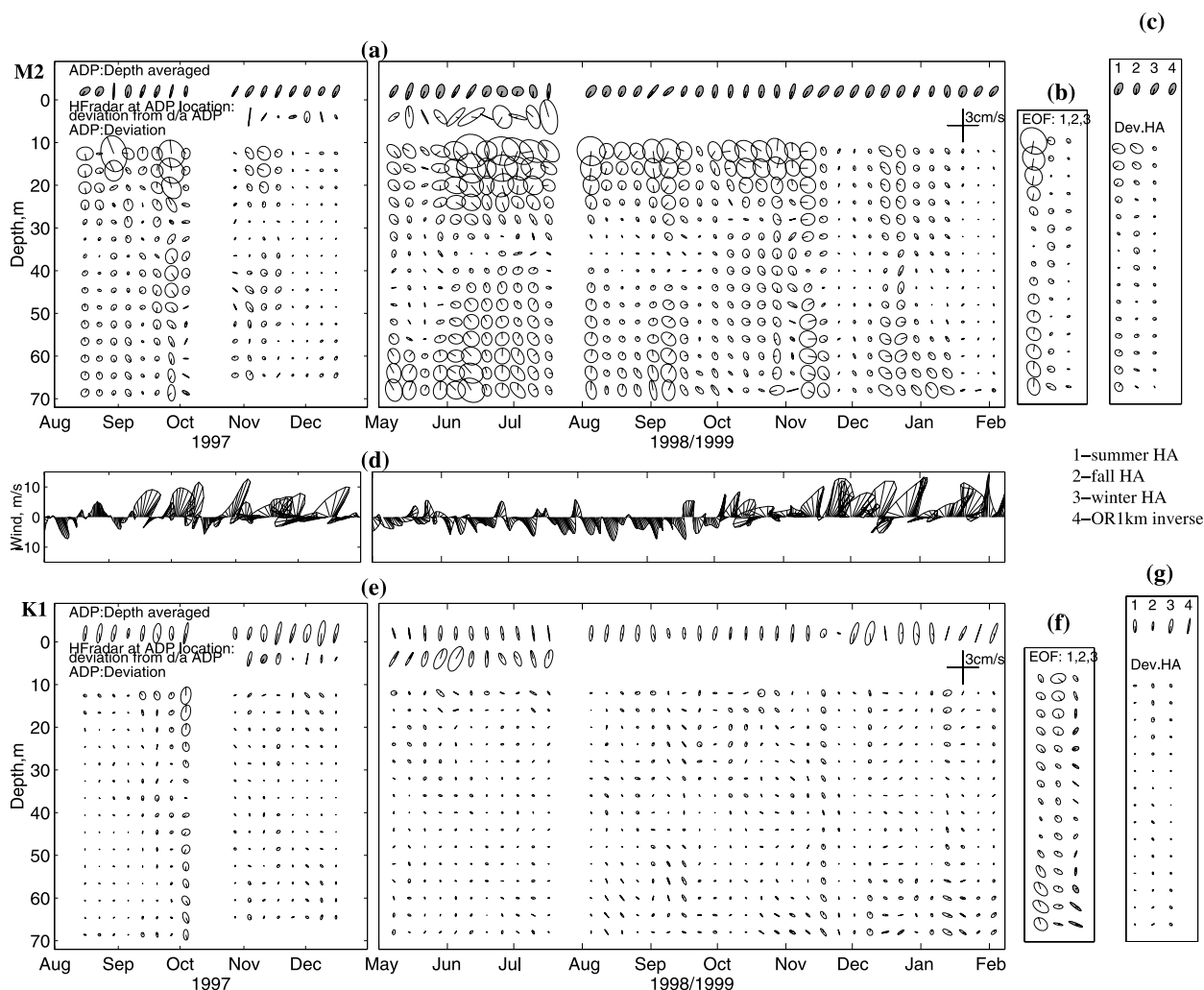


Figure 4. Tidal ellipses for ADP and nearest HF radar bin estimated for (a–c) M_2 and (e–g) K_1 in sliding 2-week windows. The upper rows in Figures 4a and 4e corresponds to depth-averaged ADP harmonic constants. Shading denotes CW rotation; no shading denotes CCW rotation. Deviation from depth-averaged ADP for available HF radar data nearest the ADP location is shown in the second row of Figure 4a for M_2 , and Figure 4e for K_1 . Deviations from the depth average over the ADP profile are plotted as functions of depth beneath this. The first three EOFs for the baroclinic variations (scaled by the corresponding mode amplitude) are plotted in Figures 4b and 4f for M_2 and K_1 , correspondingly. Seasonal harmonic analysis ellipses are shown in Figure 4c for M_2 and in Figure 4g for K_1 . Daily averaged wind vectors at Newport are shown in Figure 4d.

gimson and Hickey [1979], who analyzed data from the Coastal Upwelling Experiment (CUE) from summer 1973, and found the semidiurnal tide to be strongly baroclinic in this area. In the winter months internal semidiurnal tide amplitudes become much smaller, and are often negligible compared to the depth-averaged component.

[29] Taking summer to be May 1 to September 15, fall September 15 to October 31 and winter November 1 to January 31, we used a conventional harmonic analysis approach to estimate seasonal average tidal current ellipses. Depth averages and deviations from these averages are shown in Figure 4c for each season, and for the whole observation period. Harmonic constants for the depth-averaged currents are also given in Table 1 for each season and for the full time period, along with the corresponding results from the local prior model. Error bars for the depth-

averaged seasonal ADP harmonic constants (Table 1) were estimated using a Jackknife approach [e.g., Efron, 1981].

[30] For semidiurnal constituents (M_2 and S_2) harmonic constants for depth-averaged tidal currents vary only slightly between seasons (Table 1). However, there are persistent seasonal variations in the baroclinic signal (Figure 4c). For summer the seasonal average baroclinic currents have amplitudes comparable to or even larger than the depth average, with a profile that is strongly dominated by the first EOF. There is thus a phase locked, approximately first-mode, component of the internal tide that persists throughout the summer. Variations about this constant component are of comparable magnitude, and include modulations in amplitude and phase of the first mode, as well as more variable higher mode components. Interestingly, in the fall the average baroclinic estimates are dominated by the second

would be expected from the greater variability of the two week estimates. Seasonal averages of the depth variations are quite small (Figure 4g).

[35] Diurnal tidal currents tend to be depth independent on the central Oregon shelf at all times. However, there is significant temporal variability in the amplitude and phase of the currents, and there is enough persistence in these variations to make even estimates based on 3 or 4 months of data highly variable. This makes the definition of harmonic “constants” somewhat problematic, and suggests that estimates based on short time series, for example, those for essentially all of the historical current meters, should be treated with great caution. *Crawford and Thomson* [1984] and *Cummins et al.* [2000] have shown that there are significant seasonal variations in diurnal tidal currents on the broad shelf off Vancouver Island, and have related these modulations to seasonal changes in stratification and mean flow. While diurnal tidal currents on the shelf may be nearly depth independent (and hence at least locally consistent with the shallow water dynamics we consider here), there may still be depth variations in deeper water. Changes in stratification could thus modulate depth-averaged harmonic constants on the shelf by changing the boundary conditions at the shelf break. Since stratification off the Oregon coast is generally weakest in the winter it is likely that winter data should also be preferred for the estimates of diurnal barotropic tidal harmonic constants that we will assimilate into our barotropic model.

4.3. HF Radar Array Data

[36] The two site HF radar system provides hourly time series of radial velocities for a total of 1113 bins (Figure 1b). Harmonic constants can in principal be estimated at each of these locations, and the results can be assimilated into the barotropic tidal model. However results of harmonic analysis for individual bins are noisy (especially for short time windows), and because the radial direction varies from site to site, are difficult to analyze spatially or compare to harmonic constants for velocities in a fixed Cartesian coordinate system. For much of our analysis of the HF radar data we thus focus on the central area where radial vectors from both HF radar systems overlap so that both components of the tidal velocity vector can be resolved. To further reduce noise the overlap area (outlined in Figure 1b) was divided into 206 bins, each of approximate dimension 3.9×5.5 km, elongated alongshore. All radial data falling within each of these larger bins, and within each time window, were then fit by least squares to estimate u and v harmonic constants. For our initial analysis, 2-week time windows were used, as for the ADP data. In this case, the admittance approach described above was used to reduce the number of free parameters in each spatial bin/time window. More conventional harmonic analysis methods were used to obtain seasonal estimates for HF radar harmonic constants, with the data divided as suggested by the analysis of the ADP time series (winter, November 1997 to February 1998; spring, March to April 1998; and summer, May–July 1998).

[37] To estimate error bars for the HF radar array, two possible sources of error were considered. First, to account for temporal variability and the frequent significant gaps in time series we used a Jackknife procedure [*Efron and Tibshirani*, 1986], deleting 1 day of continuous data for

each pseudo-value. Second, variability due to random spatial sampling was estimated using a Bootstrap procedure [*Efron*, 1981], sampling (with replacement) the same number of contributing sites from each HF radar in each bin. For the winter harmonic constants, total error ranges, obtained by summing the two variance estimates for each bin, were 0.2–0.5 cm/s for the cross-shore component and as much as 0.5–1.5 cm/s for the alongshore component. Error bars were about the same for summer data and considerably larger for spring data (1–2 cm/s and 3–5 cm/s for cross-shore and alongshore components). These error bars account only for random variability; any persistent seasonal average component of data error (e.g., persistent baroclinic tidal currents) would not be included in these error estimates. For the data assimilation (based only on winter data) we take 1 cm/s as a typical total error.

[38] Since the ADP is located inside the area of overlapping HF radar coverage, direct comparison with the nearest bin is possible. Tidal ellipses for this bin are plotted in Figures 4a (M_2) and 4e (K_1) for the period when data are available from both sources. For consistency with the ADP ellipse plots, ADP depth averages were subtracted from the HF radar estimates, which should thus be most directly comparable to the top ADP bin at 12 m depth. For M_2 the residual HF radar ellipses are much smaller in the brief period of winter overlap than in the summer. RMS residuals for the surface tidal currents are 1.0 cm/s for cross-shore and 2.0 cm/s for alongshore components in winter 1997, and 3.5 cm/s for both velocity components for summer 1998. There is generally a good correlation between the HF radar residual ellipses and those from the uppermost ADP bin, especially in the summer where baroclinic signals are strong. The summer HF radar measurements are thus clearly contaminated by a significant semidiurnal internal tide and are likely to be of limited value for assimilation into our barotropic model. Of course this also means that the HF radar data may be very useful for assimilation into a stratified coastal model which can represent internal tides [*Kurapov et al.*, 2002].

[39] K_1 residual tidal ellipses for the HF radar data nearest the ADP site (Figure 4e) are noticeably smaller in winter, with RMS residuals of 0.8 cm/s for cross-shore and 2.0 cm/s for alongshore components, compared to 2.0 cm/s and 3.5 cm/s for summer 1998. In this case there is no significant correlation with the ADP residual in the uppermost bin. Thus, while there is no indication from the ADP data for seasonal variations in diurnal baroclinicity, surface currents measured by the HF radar appear to be less representative of depth-averaged currents in summer than in winter. The significant deviations of surface currents from depth averages observed in the summer apparently do not extend to significant depths. One possible explanation is that in summer a fairly regular diurnal sea breeze develops, resulting in significant near surface shear which contaminates surface currents in the diurnal band.

[40] Harmonic constants were estimated for four major constituents, for u and v , for each season, in each bin. Consistent with the results of Figure 4, the HF radar harmonic constants for the ADP bin are most consistent with the depth-averaged estimates in winter, particularly for the larger alongshore components (Table 1). Agreement is sometimes poor for other seasons. HF radar

estimates for spring are particularly erratic and have large error bars.

[41] In-phase and quadrature components of harmonic constants estimated from the winter HF radar array data are given for M_2 in Figures 5a–5b and for K_1 in Figures 6a–6b. Note that only the central $12 \times 12 = 144$ bins of the HF radar array are shown. Estimates vary smoothly over this area for both constituents. Comparison with the local prior model of Figure 3 already reveals generally good agreement between the model and the HF radar data. We examine the agreement in more detail in the next section.

[42] To better understand spatially coherent variations in the time-resolved HF radar harmonic constants, we used an EOF approach. Rather than subtract a temporal mean from the time sequence of HF radar harmonic constants, we take the winter harmonic analysis results of Figures 5a–5b and 6a–6b as an estimate of the barotropic tidal currents, and subtract this from the harmonic constants for each time window. An EOF analysis was then conducted on the spatial and temporal variations of the resulting residual harmonic constants. The first two spatial modes for each constituent are plotted as non-dimensional vectors in Figures 5c–5f and 6c–6f. Average amplitudes of the residual current modes are 1.2 cm/s and 0.5 cm/s, but this is quite variable in time (Figure 5g–5h and 6g–6h). In the first EOF for M_2 , which explains 35% of the residual variance, the surface currents have a consistent direction and phase along an axis oriented toward the northeast. The in-phase and quadrature plots (Figures 5c and 5d, respectively) give surface currents at $t = -T/4$ and $t = 0$, where T is the tidal period. Hence at $t = -T/4$ (when the current vectors of Figure 5c are reversed) the peak in southeasterly current vectors at $t = 0$ (Figure 5c) has moved to the southeast. Thus the first EOF is dominated by a wave with a crest that propagates toward the south and toward the coast with a wavelength of the order of 40 km. The second EOF for M_2 (15% of residual variance) has a generally similar, if less distinctive, wave-like character. Both of these spatial modes are consistent with an internal tide signal in the HF radar surface currents. Note that the first mode baroclinic Rossby radius computed for typical summer stratification on the Oregon shelf is about 7–8 km, roughly consistent with the observed wavelength. Temporal amplitudes of these EOFs (Figures 5g–5h) are smallest in the winter months, as would be expected from our use of the winter harmonic analysis to define the reference barotropic currents. However, amplitudes remain small through most of the spring, becoming consistently large only around May 1, with further increase in amplitude in June and July. Comparison to daily averaged wind vectors shows that the increase in EOF 1 and 2 amplitudes is coincident with the onset of persistently upwelling favorable winds. We conclude that there is clear evidence for a strong internal tide signal in the HF radar data during late spring and summer when winds are upwelling favorable. Note also that there is at least some coherence in the phase of the coefficients for the dominant EOF modes (Figures 5g–5h). All of these results are consistent with our tidal analysis of the ADP data (Figure 4), and suggest that the HF radar data will be useful for mapping internal tides on the shelf. Further efforts in this direction are reported elsewhere [Kurapov *et al.*, 2003].

[43] For the K_1 constituent the first EOF mode (Figures 6c–6d), which explains 56% of the residual variance, has very large scale, and in fact looks rather similar to the winter barotropic harmonic constants. (Note that the phase of the EOF is arbitrary, and average amplitudes of first and second mode residual currents are 2.9 cm/s and 0.6 cm/s.) This implies that over the small area covered by the overlapping HF radar data, the diurnal tidal currents are always relatively uniform (and dominantly along shore), but with temporally modulated amplitude and phase. Amplitudes for the first EOF (Figure 6g) increase significantly around the beginning of March, well before the onset of upwelling favorable winds changes the shelf stratification. After May the phase of the first EOF becomes very stable. In fact, in the summer the diurnal band harmonic constants are more stable and less noisy than in the winter. It is tempting to suggest that we are observing seasonal variations of diurnal depth-averaged tidal currents due to stratification or mean flow induced changes in phase velocity of shelf waves, as reported for Vancouver Island by Crawford and Thomson [1984] and Cummins *et al.* [2000]. However, in the summer months consistency between the HF radar and ADP data is significantly reduced in the diurnal band (Table 1) and there is a suggestion (Figure 4e) of significant shear near the surface. It is thus perhaps more likely that other non-tidal ocean motions contaminate the HF radar data in the summer, making it less useful for tidal studies. This could be related to the occurrence of a significantly more regular nearly diurnal sea breeze during the summer months, but this issue needs further study. The second EOF for the diurnal constituents is much smaller, explaining only 10% of the variance.

[44] In summary, the HF radar data is reasonably consistent with the ADP data, with surface currents from winter months most likely to be representative of depth-averaged currents and hence most useful for assimilation in our barotropic model. For assimilation we use tidal current harmonic constants (resolved into u and v components) from the 206 bins in the overlap area (Figure 1b). In principle we could directly use radial harmonic constants from the two HF radar receivers. However with the current data in more conventional Cartesian form model/data comparison and analysis of the inverse solution is more transparent and straightforward. Moreover, harmonic constants obtained by either approach represent essentially the same data (at least within the overlap domain), and experiments with inversion of HF radar radials always yielded very similar results.

4.4. Current Meters

[45] Seventeen historic current meter moorings, at locations shown in Figure 1b, were used for validation of the local models. Time series were generally short (1–3 months), with currents sampled once per hour at only three to four depths, too few to provide accurate estimates of depth averages. Furthermore, most of these moorings were occupied during summer months, when strong baroclinicity in the semidiurnal band is observed in the ADP and HF radar data. In an effort to minimize contamination by baroclinic and nontidal signals, we used the admittance approach for initial data analysis. Time windows were selected when currents appeared most barotropic, and most consistent between nearby sites. Record lengths and starting dates for the selected time series are given in Table 2. The time series

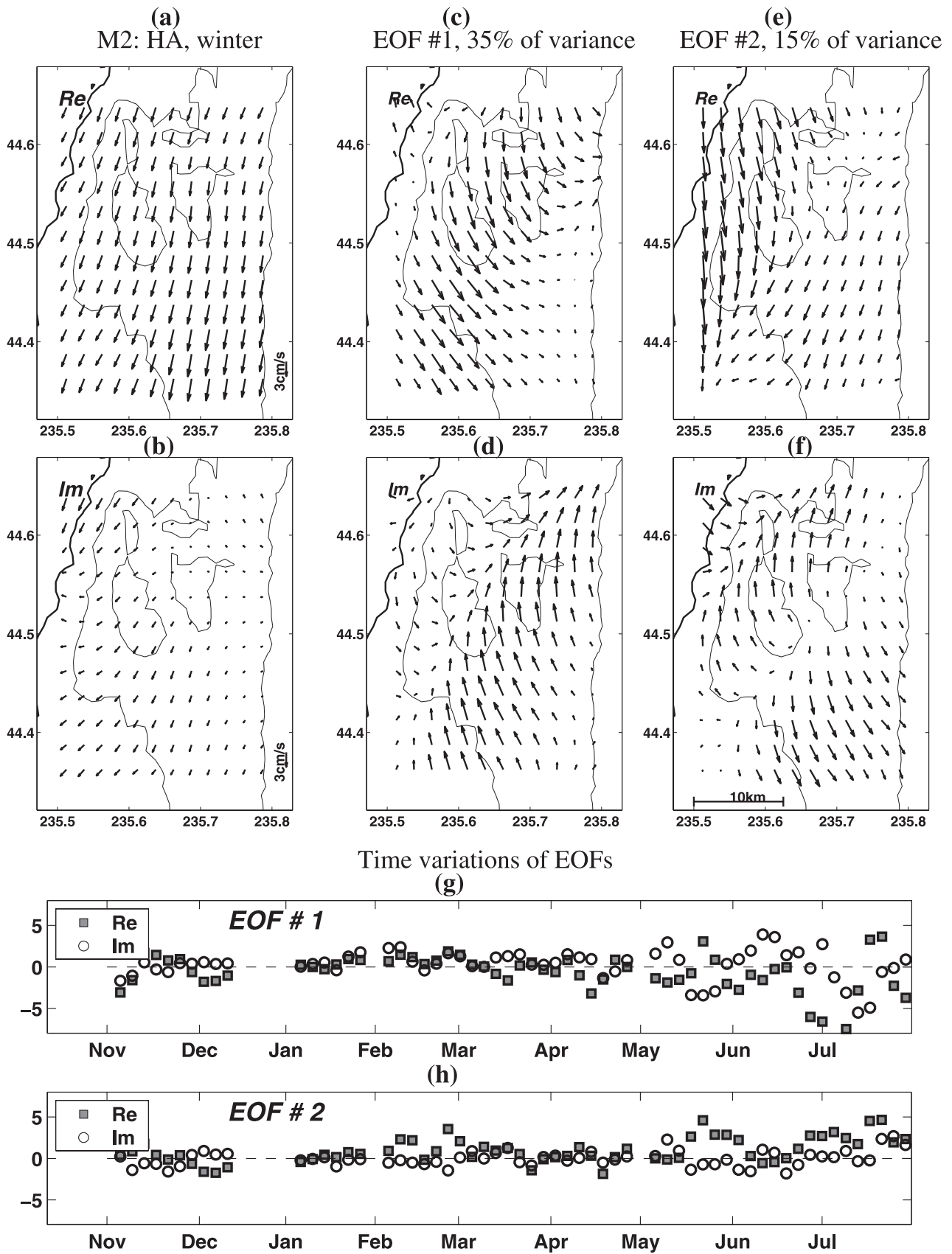


Figure 5. M_2 harmonic constants for (a) in-phase and (b) quadrature currents for winter HF radar data. (c–f) In-phase and quadrature currents for the first two spatial modes; (g–h) the corresponding temporal variations.

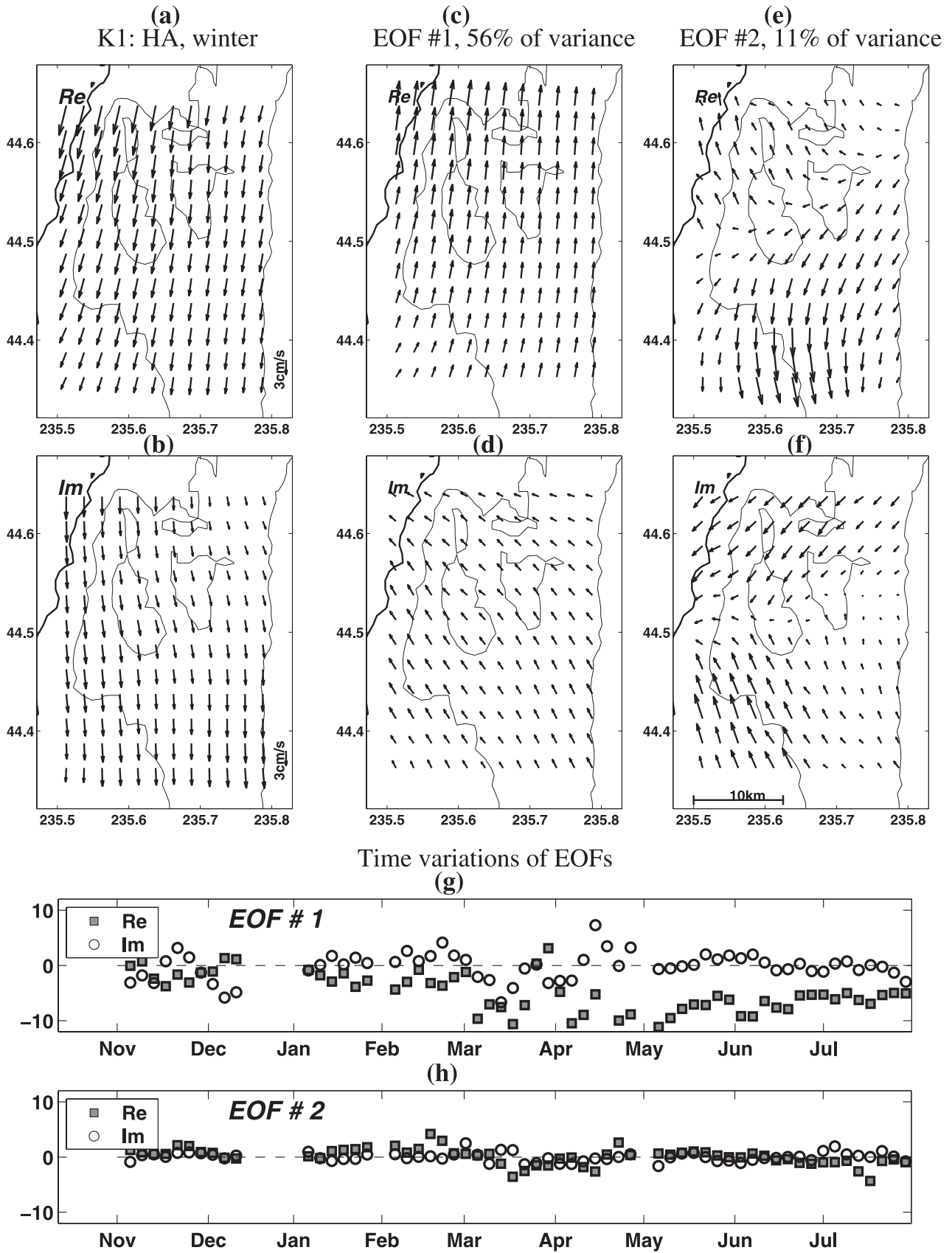


Figure 6. K_1 harmonic constants for (a) in-phase and (b) quadrature currents for winter HF radar data. (c–f) In-phase and quadrature currents for the first two spatial modes; (g–h) the corresponding temporal variations.

were averaged over depth, high-pass filtered and harmonically analyzed. The resulting tidal velocity harmonic constants are given in Table 2, grouped into four general geographic areas. To estimate error bars, we try to account for both temporal variability and the incomplete sampling in depth of the moorings. The first component was estimated using a Jackknife approach by deleting data in 12-hour segments. The second component of error was estimated by sampling the summer ADP data at random depths within three nonoverlapping ranges, chosen to match depths of the historical current mooring. The two error variances were then added to estimate total error, which is given in Table 2.

5. Local Domain Inverse Solutions

[46] We conducted a large number of assimilation experiments using the data sources described in section 4, with a range of model parameters, boundary conditions and covariance assumptions. Here we focus on two cases: inversion of HF radar harmonic constants for *u* and *v*, estimated for the 206 bins in the central part of the array where coverage from the two systems overlaps; and inversion of harmonic constants for depth-averaged tidal currents at the single ADP site. For both of these cases, only winter data were used, and all model parameters open boundary conditions, and error covariances are as described in section 2. Lessons learned from some variants on these two cases will also be discussed briefly in the following.

[47] For all inversions, we simultaneously fit all TOPEX/Poseidon altimeter data within the local model domain, along with the particular set of tidal current harmonic constants. When only current data were fit, elevations in the inverse solution were significantly degraded relative to the prior. Even very small changes in velocities can result in a very large change in the divergence of volume transports (and hence surface elevations), particularly in a small domain, and when normal flow boundary conditions are used. Explicit constraints (either as data or as boundary conditions) were required to constrain tidal elevations in the inverse solution.

[48] The error covariances control the relative fit to data and dynamics, and thus the inverse solution. The covariances also represent a specific, though compound, null hypothesis: (1) that the shallow water equations adequately capture the barotropic tidal dynamics within our local domain, subject only to minor uncertainties in bathymetry, open boundary conditions and our parameterization of friction; and (2) that our estimated harmonic constants are representative (within the specified error bars) of depth-averaged tidal currents. If we can simultaneously fit both data and dynamics within the assumed error levels, this hypothesis cannot be rejected. Assuming all covariances are correctly specified, and that all errors (in data and dynamics) are Gaussian, the reduced penalty functional can be shown to have a chi-square distribution with *N* (= number of data) degrees of freedom [e.g., Bennett, 1992]. This allows a completely rigorous statistical test of the null hypothesis. However, the validity of this test depends on a number of assumptions about error distributions and covariances that are difficult to verify, or even justify. For example, we have assumed that data errors are uncorrelated. For the gridded and averaged HF radar data we consider here this assump-

Table 2. Harmonic Constants for Historic Current Meters^a

Area	Lat	Lon	Experiment	Recl., Starting days	date	M2			S2			K1			O1						
						U	V	Phase	U	V	Phase	U	V	Phase	U	V	Phase				
CA	44.650	235.715	CUE1	27	07.06.72	3.7±0.8	156±14	4.4±1.0	198±14	1.4±0.6	183±25	1.7±0.8	225±39	1.3±0.8	N/D	6.4±1.3	227±18	0.7±0.9	N/D	3.6±1.5	211±28
	44.745	235.713	CUE1	25	07.20.72	2.4±0.7	159±18	3.6±0.9	201±16	0.9±0.5	186±33	1.4±0.7	227±43	0.6±0.8	331±88	3.8±1.3	216±25	0.4±0.9	N/D	2.2±1.4	200±39
	44.643	235.475	CUE1	28	07.06.72	4.4±0.7	156±10	3.9±0.8	157±13	1.7±0.5	183±17	1.5±0.6	184±23	0.6±0.7	N/D	3.4±0.8	196±15	0.4±0.8	N/D	1.9±1.0	180±31
NSD	45.277	235.040	SUCS	116	01.24.78	0.9±0.2	164±14	2.9±0.3	191±7	0.0±0.2	N/D	0.9±0.3	233±32	0.2±0.2	138±78	1.4±0.3	172±13	0.2±0.3	224±120	0.8±0.4	147±35
	45.352	234.350	SUCS	114	05.23.78	0.6±0.5	192±49	2.7±0.5	207±12	0.2±0.2	219±74	1.0±0.2	233±20	0.0±0.2	N/D	1.0±0.2	207±13	0.0±0.2	N/D	0.6±0.2	191±20
	45.355	234.362	SUCS	42	01.26.78	0.5±0.5	190±59	3.5±0.5	200±9	0.1±0.2	N/D	1.3±0.2	226±13	0.2±0.2	24±63	0.9±0.2	200±14	0.1±0.2	N/D	0.6±0.2	174±20
NSM	44.988	235.618	SUCS	70	01.27.78	1.8±0.3	120±20	1.7±0.4	152±16	0.7±0.3	147±30	0.7±0.4	179±33	0.6±0.3	131±44	0.9±0.3	177±20	0.3±0.3	115±136	0.5±0.4	161±49
	44.988	235.269	WISP	94	04.26.75	1.5±0.5	121±38	1.9±0.5	160±17	0.6±0.3	148±34	0.7±0.3	187±25	0.8±0.2	70±42	1.6±0.2	189±8	0.4±0.2	75±111	0.7±0.2	194±17
	45.270	235.688	CUE2	37	07.22.73	2.9±0.6	124±22	2.9±0.6	156±13	1.1±0.4	150±25	1.1±0.4	183±21	1.1±0.3	161±17	1.2±0.3	199±16	0.6±0.3	145±35	0.7±0.3	183±25
NSS	45.280	235.340	CUE2	28	07.14.73	1.4±0.6	109±76	0.6±0.6	132±86	0.5±0.3	136±48	0.2±0.3	159±93	0.6±0.3	150±34	1.4±0.3	206±14	0.3±0.3	134±83	0.8±0.3	190±22
	45.003	235.617	WISP	89	01.28.75	2.1±0.4	145±14	2.3±0.4	185±11	0.9±0.4	170±26	0.9±0.4	211±30	0.9±0.5	120±64	0.7±0.5	209±47	0.6±0.5	65±113	0.8±0.5	170±37
	44.855	235.800	CUE1	25	07.07.72	2.2±0.5	150±16	3.3±0.6	172±11	0.4±0.3	68±115	1.3±0.3	282±64	0.5±0.3	35±42	3.9±0.3	246±11	0.6±0.3	185±29	2.4±0.3	180±8
NSM	44.997	235.837	WISP	92	04.27.75	1.4±0.5	151±24	2.2±0.6	205±18	0.6±0.3	178±29	0.9±0.3	232±64	1.0±0.3	164±18	1.8±0.3	235±17	0.4±0.3	191±44	0.7±0.3	222±34
	44.996	235.848	WISP	45	07.29.75	1.4±0.6	161±02	2.4±0.6	220±19	0.3±0.4	194±79	1.2±0.4	232±32	0.3±0.4	N/D	1.1±0.5	222±36	0.2±0.4	N/D	0.6±0.5	225±68
	45.180	235.918	CUE2	33	07.24.73	1.6±0.7	120±51	1.3±0.7	147±37	0.6±0.5	115±113	0.5±0.4	173±58	1.5±0.4	129±25	0.8±0.4	200±31	0.9±0.4	113±66	0.4±0.4	184±58
NSM	45.270	235.885	CUE2	59	06.30.73	0.8±0.6	129±69	2.3±0.6	180±15	0.3±0.4	156±84	0.9±0.4	206±29	0.6±0.4	165±40	1.2±0.4	188±20	0.4±0.4	149±67	0.7±0.3	172±25
	45.582	235.852	CUE2	36	07.22.73	2.8±0.7	142±19	3.1±0.7	155±15	1.6±0.5	178±18	1.4±0.5	164±22	0.9±0.4	236±46	2.3±0.4	192±11	0.8±0.4	141±37	1.1±0.4	150±25

^aAmplitude is in centimeters and phase is in degrees.

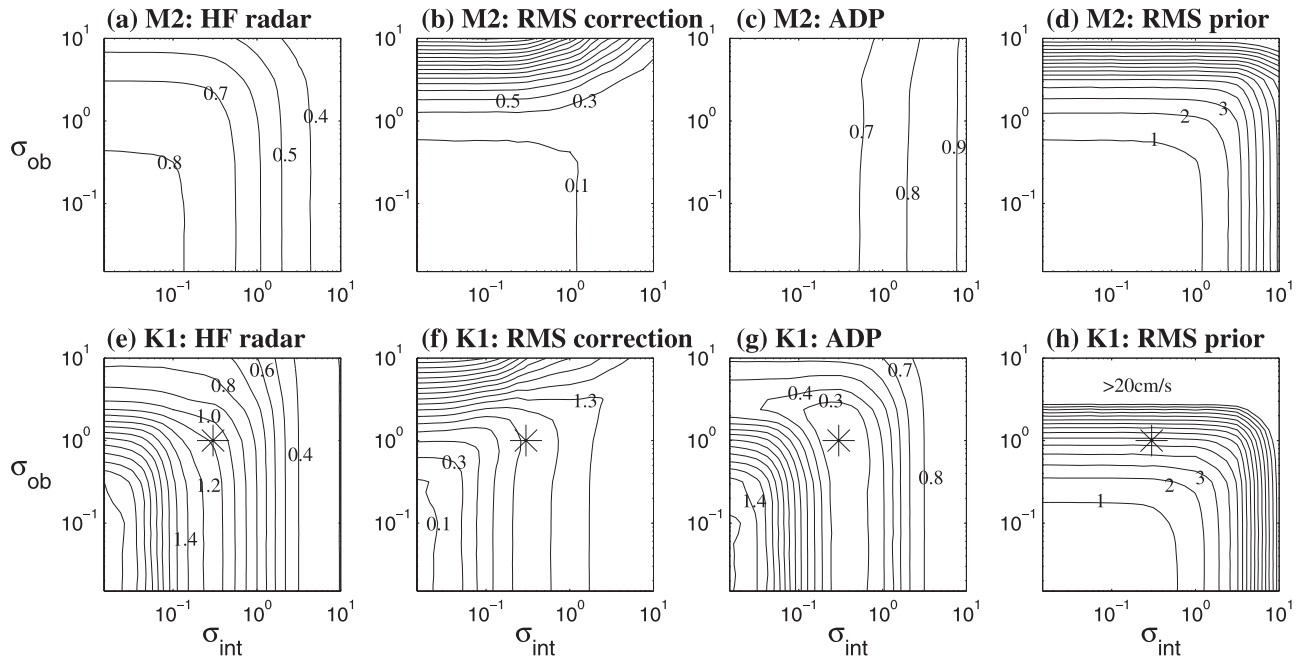


Figure 7. Contour plots of inverse solution misfits and model variance for the M_2 and K_1 as a function of σ_{int} and σ_{ob} . (a, e) RMS misfit for HF radar data; (b, f) RMS difference between currents in the inverse and prior models (averaged over the domain); (c, g) RMS misfit with depth-averaged ADP harmonic constants; (d, h) RMS prior error in the currents (averaged over the domain).

tion is almost certainly not reasonable. However, it is not obvious how to estimate accurately the magnitude of errors in the HF radar harmonic constants much less the full covariance. Developing a realistic model for the dynamic error covariance is a much more daunting task. We thus adopt a more informal approach to assess the fit of the inverse solution to data and dynamics, and to simultaneously explore the sensitivity of the inversion to the assumed error covariances.

[49] By computing representers separately for the interior dynamical equation (int) and open boundary condition (ob) penalty terms, and introducing scaling factors σ_{int} and σ_{ob} for the corresponding error terms, inverse solutions can be computed efficiently for a two-parameter family of error covariances [e.g., Kurapov *et al.*, 2002]. The effect of varying the assumed magnitude of these dynamical error scales, while keeping the assumed data error level fixed at 1 cm/s for all HF radar data, is illustrated in Figure 7 for the HF radar array inversion. RMS misfits to the HF radar data for the M_2 and K_1 inverse solutions are contoured as a function of σ_{int} and σ_{ob} in Figures 7a and 7e. The limiting value approached in the lower left-hand corner of these plots corresponds to the RMS misfit of the prior solution. As σ_{int} and σ_{ob} are increased, fit to the data is emphasized and the inverse solution deviates increasingly from the prior. The choice $\sigma_{\text{int}} = \sigma_{\text{ob}} = 1$ corresponds to our a priori dynamical covariance assumptions, outlined in section 2. For large values of the covariance scaling factors, we expect the solution to lose regularity, with currents increasing to unrealistically large amplitudes. This is illustrated in Figures 7b and 7f, where the RMS differences between currents in the inverse and prior models (averaged over the model domain) are contoured. In Figures 7c and 7g, we plot the RMS misfit between the inverse solution and the harmonic

constants estimated from the depth-averaged ADP data. Note that for the case illustrated in Figure 7 the ADP data is used only for validation of the HF radar inverse solution.

[50] For M_2 the prior model already fits the winter HF radar data to within the assumed data uncertainty of 1 cm/s, with the RMS misfit decreasing slowly from 0.8 cm/s (for the prior) to 0.4 cm/s with increasing σ_{int} , σ_{ob} . Very large and physically unreasonable dynamical errors would be required for any significant improvement in data fit. The prior solution for M_2 also fits the ADP tidal constants fairly well, with a RMS misfit of 0.6 cm/s. This is roughly a factor of 2 larger than the estimated error level (Table 1). Fit to the ADP is relatively insensitive to variations in the dynamical error scales assumed for the inversion (Figure 7c). Overall, the prior model already provides a reasonable fit to both data sets, and our a priori covariance assumptions appear to be completely reasonable. Choosing $\sigma_{\text{int}} = \sigma_{\text{ob}} = 1$, we obtain a regular solution, which deviates only slightly from the prior. The representers can be interpreted as the covariance of the error in the prior solution [Bennett, 1992; Egbert and Bennett, 1996]. For $\sigma_{\text{int}} = \sigma_{\text{ob}} = 1$ errors in the prior M_2 currents are only about 1 cm/s (Figure 7d), comparable to the data error magnitude. It is thus not surprising that the solution cannot be significantly improved by assimilation. Experiments with variants on the data set (e.g., using harmonic constants estimated directly from the larger set of HF radar radial currents) produced similar results. We note that the adequacy of the prior numerical model is strongly dependent on the accurate open boundary conditions obtained from the nested inverse solutions.

[51] For K_1 the situation is rather different. Now the RMS misfit to the prior solution is 2.4 cm/s, significantly greater than the estimated HF radar error bars. Increasing the error covariance scale factors allows significant improvements in

data fit, with the RMS reduced to 0.8 cm/s at $\sigma_{\text{int}} = 1$, $\sigma_{\text{ob}} = 1$, and below 0.4 cm/s for large values of σ_{int} (Figure 7e). Figure 7f shows that relative to M_2 , the K_1 inverse solution is much more sensitive to variations of the scaling factors, with relatively large currents produced at some points in the domain when σ_{int} and (especially) σ_{ob} are increased. Fit to the ADP data is also very strongly affected by the choice of these scale factors (Figure 7g). The RMS misfit to this validation data first decreases rapidly for $\sigma_{\text{int}} < 0.3$, $\sigma_{\text{ob}} < 1$ from 1.6 cm/s to 0.2 cm/s, and then increases up to 0.8 cm/s again for larger values of these factors.

[52] For our preferred K_1 inverse solution we take $\sigma_{\text{int}} = 0.3$, $\sigma_{\text{ob}} = 1$ (shown with asterisk in Figures 7e–7g) to optimize fit to the ADP data. If the assumed data error standard deviation of 1 cm/s is correct, this corresponds to a reduction by a factor of about 3 in the amplitude of model errors, relative to the covariance suggested in section 2. Alternatively, we could interpret the discrepancy (between our prior covariance and the optimal scale factor) as evidence that the data errors exceed 1 cm/s, since the inverse solution depends only on the ratio of dynamical and data error variations [e.g., Bennett, 1992]. The systematic seasonal variations in amplitude and phases of depth-averaged diurnal tidal currents at the ADP, and discrepancies between HF radar and ADP harmonic constants that typically exceed estimated error levels, both support this explanation. In fact, it is most probable that both factors contribute to the discrepancy: Model errors have probably been overestimated, and data errors underestimated. The representers calculated for $\sigma_{\text{int}} = 1$, $\sigma_{\text{ob}} = 1$ predict RMS errors in the prior solution currents exceeding 6 cm/s (Figure 7h), significantly larger than actual data/model discrepancies.

[53] We also computed inverse solutions for the S_2 and O_1 constituents, using σ_{int} and σ_{ob} determined for M_2 and K_1 , respectively. Harmonic constants at the ADP site for all four constituents are given in Table 1. For our preferred solution the total (summed over four constituents), HF radar RMS misfit goes from 2.7 cm/s (prior) to 1.6 cm/s (inverse). The total ADP RMS misfit is reduced from 2.2 cm/s to 1.0 cm/s. In general, results for S_2 were similar to those for M_2 , with the prior model already fitting the HF radar and ADP data adequately. For O_1 the agreement between the prior model and the HF radar data was much better than for K_1 . The inverse solution reduced the O_1 HF radar RMS from 1.1 to 0.7 cm/s, compared to the change from 2.4 to 1.0 cm/s for K_1 . The apparent difference in the adequacy of the dynamics for the K_1 and O_1 constituents is probably not real. In forward modeling experiments we found solutions for the diurnal constituents to be very sensitive to details of model configuration. For example, slightly increasing the alongshore extent of the model domain resulted in a prior solution for K_1 that was in much better agreement with the HF radar data, while the fit to O_1 was significantly degraded. Changes in the friction parameterization also had a very large effect on the prior solutions for diurnal constituents. In all of these cases, inverse solutions incorporating HF radar data were very similar, both for the K_1 and O_1 constituents, demonstrating the value of the surface current data in constraining barotropic tidal velocity fields near the area of data coverage.

[54] In-phase and quadrature currents for the K_1 inverse solution are shown in Figures 8a and 8b. For M_2 the inverse

solution currents are essentially identical to those already plotted for the prior in Figures 3a and 3b and are not shown here. Compared to the prior model (Figures 3c and 3d), currents for the K_1 inverse solution are significantly larger and have shorter spatial scale on the shelf, particularly over the HSBC where maximum amplitudes exceed 6 cm/s for both in-phase and quadrature components. Note that current vectors are trimmed to maximum amplitude of 3 cm/s in Figure 8. Together, the in-phase and quadrature plots suggest northward phase propagation of a short wavelength (~ 100 km) disturbance over the broadened HSBC shelf and adjacent slope, strongly suggestive of a topographically trapped shelf wave. We consider this feature further in the next section.

[55] A second inverse solution was obtained using only the ADP data, with the covariance scaling factors chosen as for the HF radar case, and the data error level set to 1 cm/s. This solution improves the overall (four constituents) HF radar array misfit from 2.7 cm/s to 1.8 cm/s, and at the same time reduces the RMS misfit to the fitted ADP data from 2.2 cm/s to 0.6 cm/s. As for the HF radar inversion, there is little change from the prior for the semidiurnal currents, but very significant changes for the diurnal currents. Results for K_1 are plotted in Figures 8c and 8d. The similarity to the HF radar inversion is rather remarkable, given that only a single data point was used for the inversion.

[56] In Figure 9, we compare harmonic constants estimated from the historic current meter moorings (Table 2) to the inverse solution in the northern half of the local domain, where all of the current meters were located. Except for three current meters from CUE1 (in the geographic area denoted by CA in Figure 9 and Table 2), these do not overlap with the HF radar array. For M_2 , agreement with the inverse solution (and the prior) is generally quite good everywhere. The spatial complexity seen in the inverse solution quadrature component on the shelf is at least qualitatively consistent with these validation data. For K_1 the fit of the inverse solution is not quite as good. RMS misfits for the prior and inverse models are similar for all geographical subsets except for CA, where the RMS misfit for the alongshore component goes from 3.4 cm/s for the prior to 1.6 cm/s for the inverse. The historical current meters in this area verify that diurnal tidal currents are intensified over the broadened shelf near the HSBC, although the reversal in direction of the quadrature component predicted by the inverse solution in the southern part of this area is not observed. Given the seasonal variability of harmonic constants for depth-averaged diurnal currents (Table 1, Figure 4g), it is not surprising to find some disagreement between the inverse solution (based only on winter data), and current meter data collected over a range of seasons (but mostly in summer months).

6. Discussion

[57] An alternative view of the tidal currents on the central Oregon shelf is provided in Figure 10, where amplitudes and phases of clockwise (CW) and counterclockwise (CCW) rotary currents are plotted for the M_2 and K_1 inverse solutions. These are formed in the usual way from the Cartesian u-v representation of the currents as $u + iv$ and $u - iv$, for CW and CCW components,

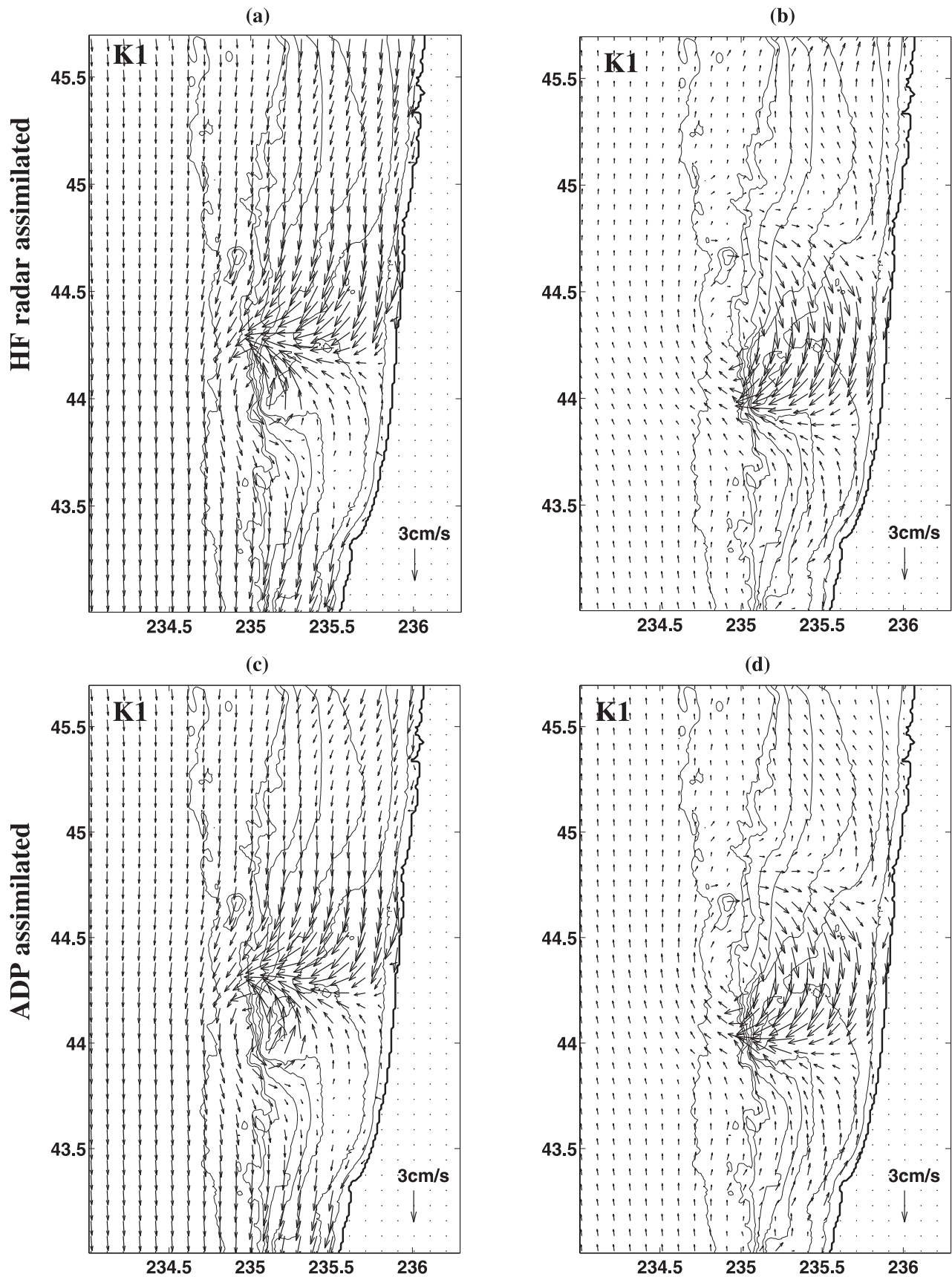


Figure 8. (a) In-phase and (b) quadrature currents for the solution assimilating HF radar data. (c) In-phase and (d) quadrature currents for the solution assimilating depth-averaged ADP data. Current vector magnitudes are trimmed to 6 cm/s for M₂, and to 3 cm/s for K₁.

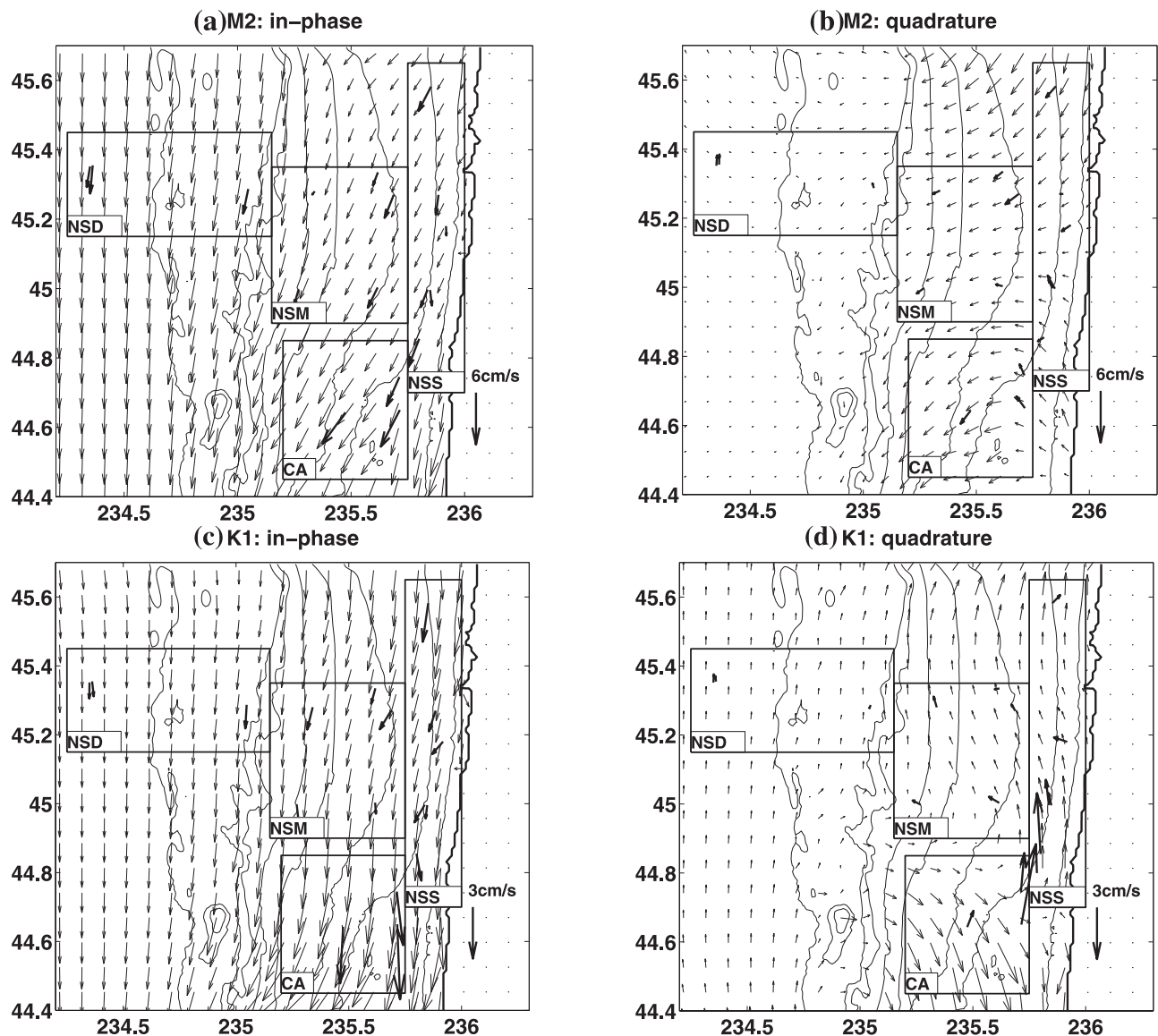


Figure 9. Comparison of historic current meters and the inverse HF radar solution. Vectors corresponding to current meter harmonic constant estimates (bold) are superposed on the inverse solution. Current meter groupings as used in Table 2 are outlined. Current vector magnitudes are trimmed to 6 cm/s for M_2 and to 3 cm/s for K_1 .

respectively (note that we assume a time dependence of $\exp\{+i\omega t\}$). For both constituents the CCW components (Figures 10a and 10c) have nearly constant phase over the local model domain, except in the area around the amphidrom for K_1 . Amplitudes for the CCW component vary by approximately 50%. The CW rotary currents show considerably more variation both in amplitude and phase (Figures 10b and 10d). Phases for the M_2 CW component (Figure 10b) decrease from 270° in deep water to about 210° or less on the shelf. This corresponds to a phase lag of one sixth of a tidal period, or a delay of about 2 hours of the deep water CW rotary currents. M_2 CW currents are more variable on the shelf than CCW currents, with the largest amplitudes over the south side of the HSBC, and near the southern edge of the domain. CW rotary currents for K_1 (Figure 10d) are the most interesting. Amplitudes peak over the outer edge of the HSBC between 100 and 200 m depth. On this section of

shelf the CW rotary phases increase uniformly to the north, by about 180° over a distance of about 60 km. North of Stonewall Bank, where the shelf narrows and shelf slopes decrease, the CW rotary amplitude decays and the phase contours become more widely spaced.

[s8] The CW currents over the HSBC clearly have the character of shelf waves (i.e., short wavelength variations of currents over the shelf and slope, northward phase propagation). To better understand the dynamics we calculated barotropic dispersion curves [e.g., Brink, 1991] for three two-dimensional (uniform alongshore) bathymetric profiles across the Oregon shelf (denoted A, B, and C in Figure 1b). The profiles and corresponding dispersion curves for first mode barotropic shelf waves are plotted in Figure 11. Only for the central profile (B) through the center of Heceta Bank does the dispersion curve reach the K_1 frequency. For this profile two first mode shelf waves are allowed at the K_1

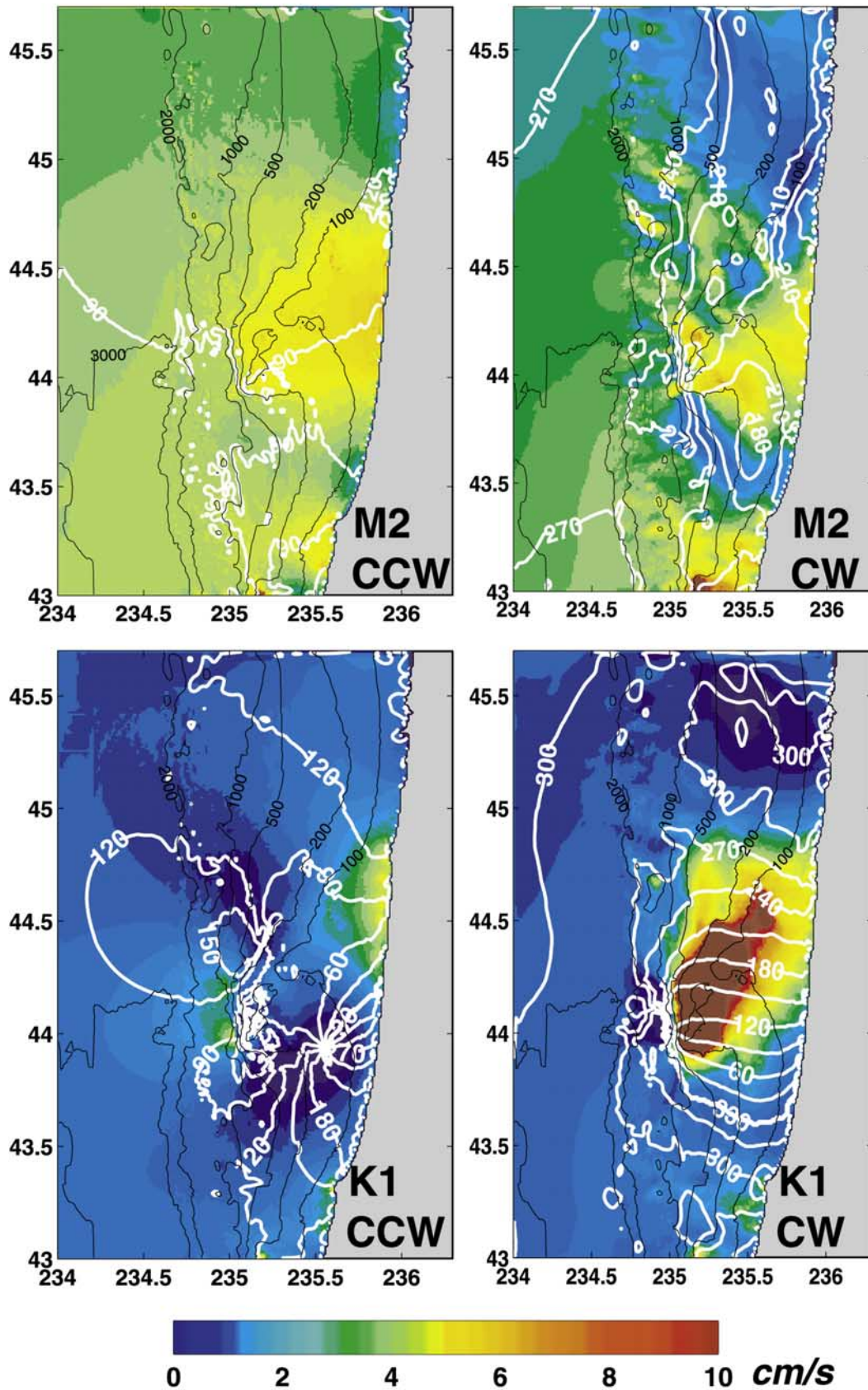


Figure 10. (left) Amplitudes and phases of clockwise $u + iv$ and (right) counterclockwise $u - iv$ rotary currents for the M₂ and K₁ inverse solutions. Phase convention is such that higher phases correspond to time delays.

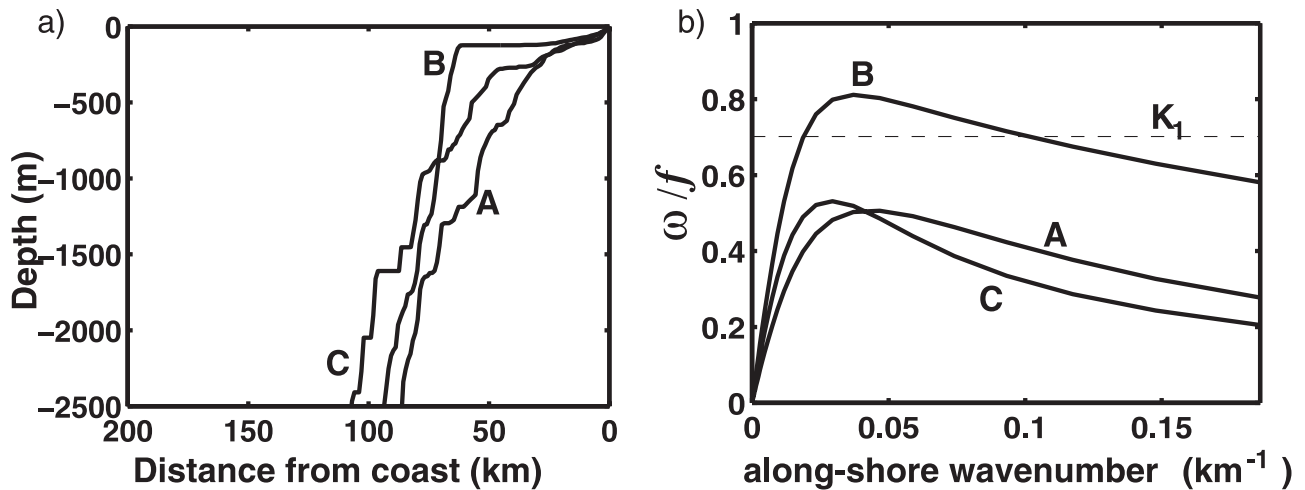


Figure 11. (a) Bathymetric profiles for cross-sections A, B, C in Figure 1b. Corresponding dispersion curves for first mode barotropic shelf waves. The dashed line in Figure 11b corresponds to the K_1 frequency.

frequency (dashed line in Figure 11b), with wavelengths of approximately 270 km and 85 km. To the north and south the shelf is too narrow (and slopes are not steep enough) to allow shelf wave propagation. Velocity ellipses for the two K_1 shelf waves permitted for the Heceta Bank profile are plotted in Figure 12, along with the ellipses for the corresponding (shelf-modified) Kelvin wave.

[59] As expected [e.g., Munk *et al.*, 1970; Crawford and Thomson, 1984] the Kelvin wave is nearly linearly polar-

ized (equal CW and CCW) in deep water, and dominantly CCW on the shelf, while the shelf waves are restricted to the shelf where they are dominantly CW. The profile of velocity ellipses for the shorter ($\lambda = 85$ km) shelf wave in Figure 12, is reasonably consistent with the CW amplitudes and phases over the outer edge of the HSBC (Figure 10d). Amplitudes of this mode in Figure 12 are strongly peaked over the steepest slopes, and decrease rapidly shoreward. In the K_1 inverse solution peak amplitudes are in somewhat shallower

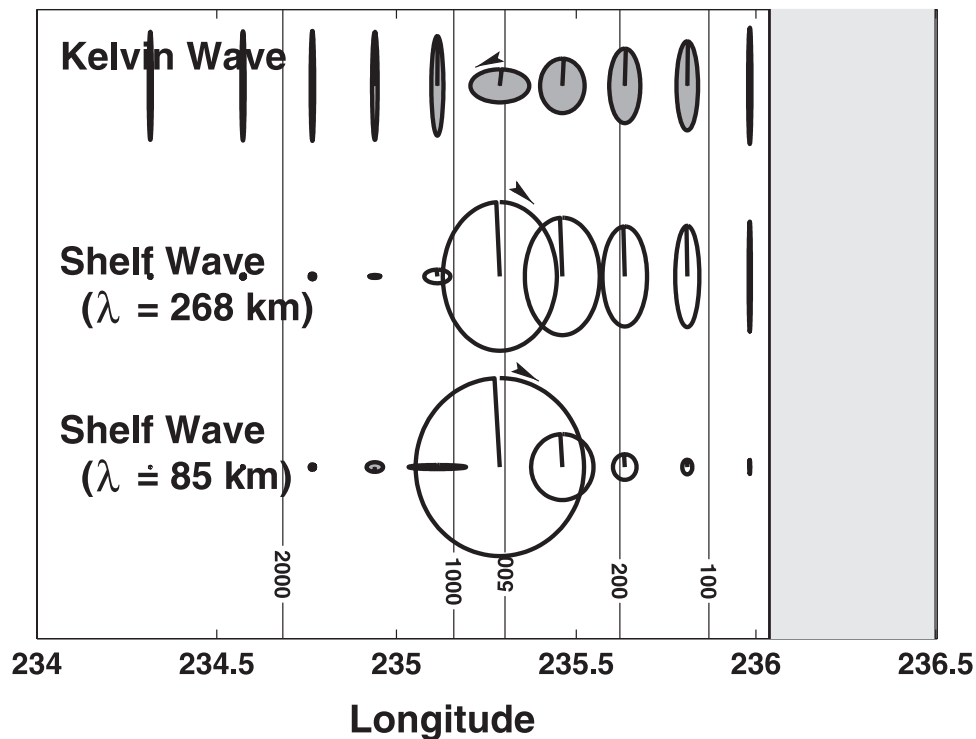


Figure 12. Velocity ellipses for the two barotropic shelf waves permitted for the Heceta Bank profile (B) at the K_1 frequency along with ellipses for the (shelf-modified) Kelvin wave (top). Shading corresponds to CCW tidal ellipse rotation. Depths for the cross-section are contoured.

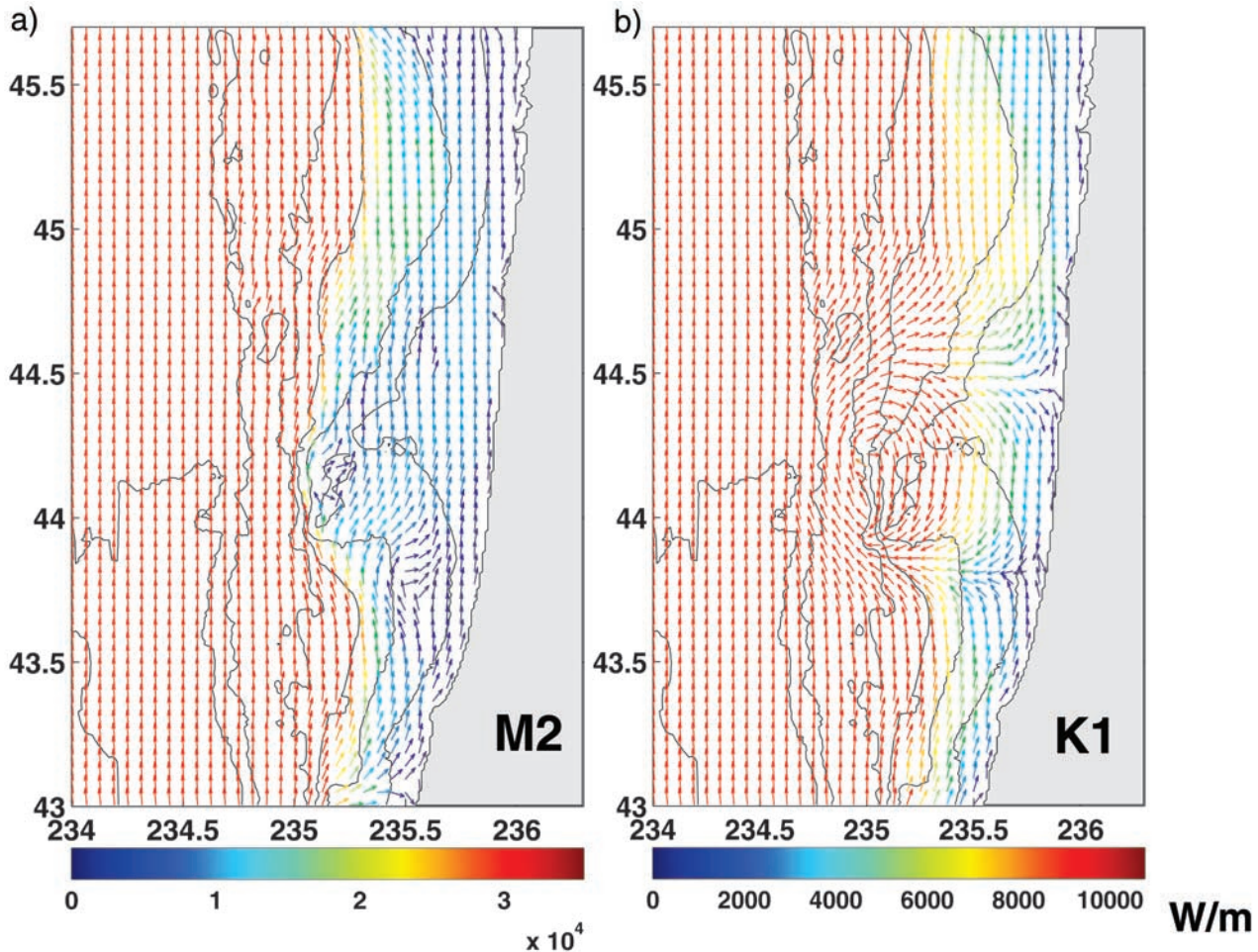


Figure 13. Depth-integrated barotropic M_2 and K_1 energy flux vectors. Magnitude, which varies significantly between deep water and the shelf, is indicated by color.

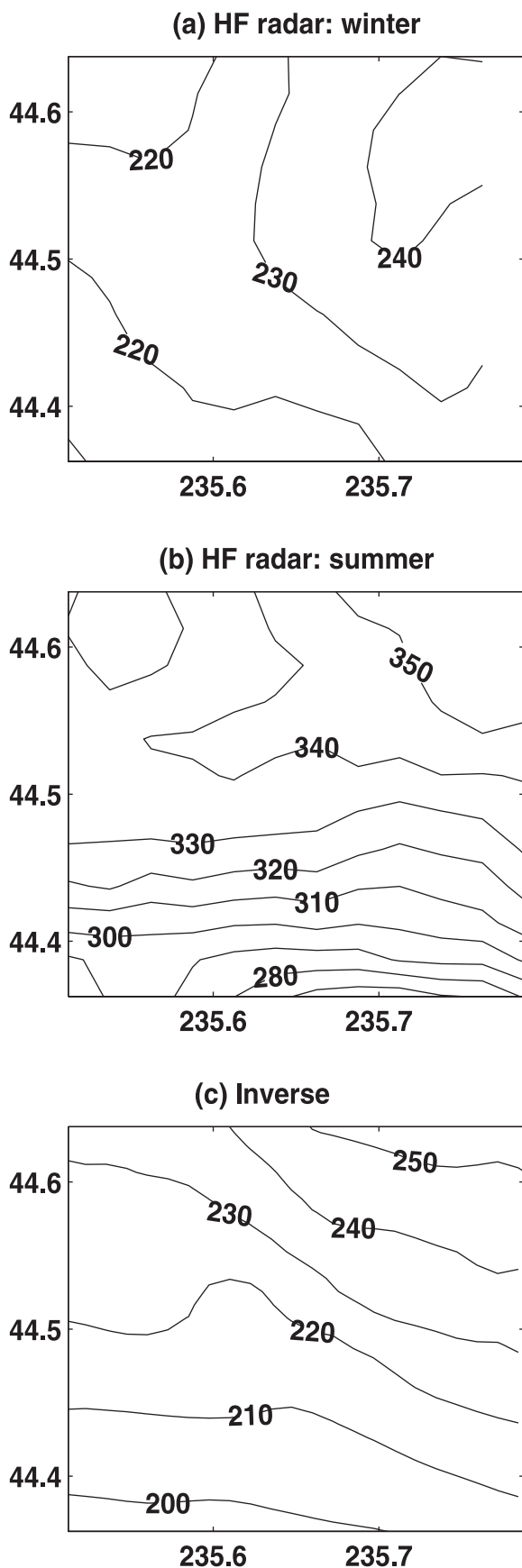
water, perhaps due to three-dimensional effects. The phase propagation in the inverse solution (180° in about 60 km) is also at least qualitatively consistent with the predicted 85 km wavelength. We thus suggest that the enhanced diurnal tidal currents around the HSBC result primarily from a topographic shelf wave on the descending part of the dispersion curve. The wave is restricted to the short section of coast (on the order of one wavelength) where propagation of this mode is allowed.

[60] Energy flux vectors computed for the inverse solution provide further support for this interpretation. Since the dispersion curve is descending for the appropriate mode, the group velocity is negative and energy flux should be to the south. This is confirmed (for the inverse solution) in Figure 13b, which reveals a complex pattern in the diurnal band over the broad shelf near the HSBC, where energy flux is indeed to the south. Note that the energy flux for the super-inertial semidiurnal constituents is by comparison very simple (Figure 13a). Although there is some deflection and steering by the topography, energy flux is always directed to the north for M_2 .

[61] While most of the Oregon shelf is too narrow to support propagating barotropic shelf waves at diurnal tidal frequencies, there are locations where the shelf widens and

slopes steepen enough to allow barotropic shelf waves. In addition to the HSBC segment in our local domain, the area around the Astoria fan (just north of the top of our local domain) also apparently allows shelf waves. This can be seen in the regional model currents of Figures 2e and 2f, and is verified by dispersion calculations for the cross-shore bathymetry profile. Because the favorable bathymetric profiles are restricted to short segments of the coast, these waves do not propagate a significant distance, but rather remain trapped near where they are excited by alongshore variations in bathymetry. Since stratification has the effect of moving dispersion curves up and to the left on the plots of Figure 11 [e.g., Brink, 1991], alongshore propagation of shelf waves may in fact be more continuous than suggested by our unstratified model.

[62] The amplitude of the shelf wave seen in the K_1 inverse solution exceeds 6 cm/s over the steep slope, farther offshore than any of the HF radar or current meter data. This specific feature thus cannot be directly verified. However, the inverse solution suggests that the shelf wave should also be evident in the phase of CW rotary currents all the way to the coast. In Figure 14, we plot CW rotary phase computed from harmonic analysis of 6 weeks of winter (November 1 to December 15, 1998) and 8 weeks of summer (June 1 to



July 31, 1998) HF radar data in the central rectangular part of the overlap area, along with the corresponding results from the inverse solution (Figure 14c). The HF radar harmonic constants show a systematic northward increase in CW rotary phase, similar to that seen in the inverse solutions. A similar pattern is seen in HF radar harmonic constants computed from other time windows, except during the spring when tidal currents become too variable to allow stable estimates of harmonic constants. The HF radar data thus provides strong evidence that shelf waves similar to those seen in the K_1 inverse solution are indeed present in the ocean over the HSBC. However, as illustrated by the differences between Figures 14a and 14b, actual CW phase values are quite variable in time, and thus must be very sensitive to changing ocean conditions such as stratification or background currents [Crawford and Thomson, 1984; Cummins *et al.*, 2000].

[63] The sensitivity of the shelf currents to details in the dynamics is also evident in the inversion results. While all inversion experiments (varying the prior solution, friction, data sets) result in some sort of shelf wave in the diurnal currents over the HSBC, details are quite variable, especially outside the area covered by the HF radar systems. Posterior error analysis for the inverse solution confirms that the shelf wave currents are not tightly constrained by the available data (Figure 15). Over the area of steep shelf beyond the HF radar coverage, posterior errors in the estimated K_1 CW rotary currents exceed 8 cm/s, larger than the estimated currents themselves. This shows that relatively small uncertainties in the (depth-averaged) dynamical equations can be expected to result in significant uncertainties in CW rotary currents on the shelf, particularly over the HSBC. Thus, while the posterior errors support our conclusion that large diurnal CW currents can easily be generated over the HSBC, our estimate of the actual amplitude and phase of currents in this area is not well constrained. Note that uncertainties for CCW rotary currents and for both M_2 rotary components also peak over the HSBC, but errors for these currents are generally less than 1–2 cm/s.

7. Conclusions

[64] Our assumption of shallow water dynamics, with no allowance for stratification or lower frequency background currents, imposes a major limitation on our study of tides off the central Oregon coast. Analysis of HF radar and ADP data clearly demonstrates that seasonal variations in ocean conditions can have a substantial effect on tidal shelf currents in both the diurnal and semidiurnal bands. A more complete 3D stratified model would allow a fuller understanding of this variability. Nonetheless, our barotropic inverse study provides some useful insights into tidal dynamics on the central Oregon shelf.

[65] In the semidiurnal band, significant but highly variable internal tides are observed in both the ADP and HF

Figure 14. (opposite) (a) CW rotary phase computed from harmonic analysis of 6 weeks of winter (November 1 to December 15, 1998) and (b) 8 weeks of summer (June 1 to July 31, 1998) of HF radar data for the central area of the local domain. (c) CW rotary phase for the inverse solution.

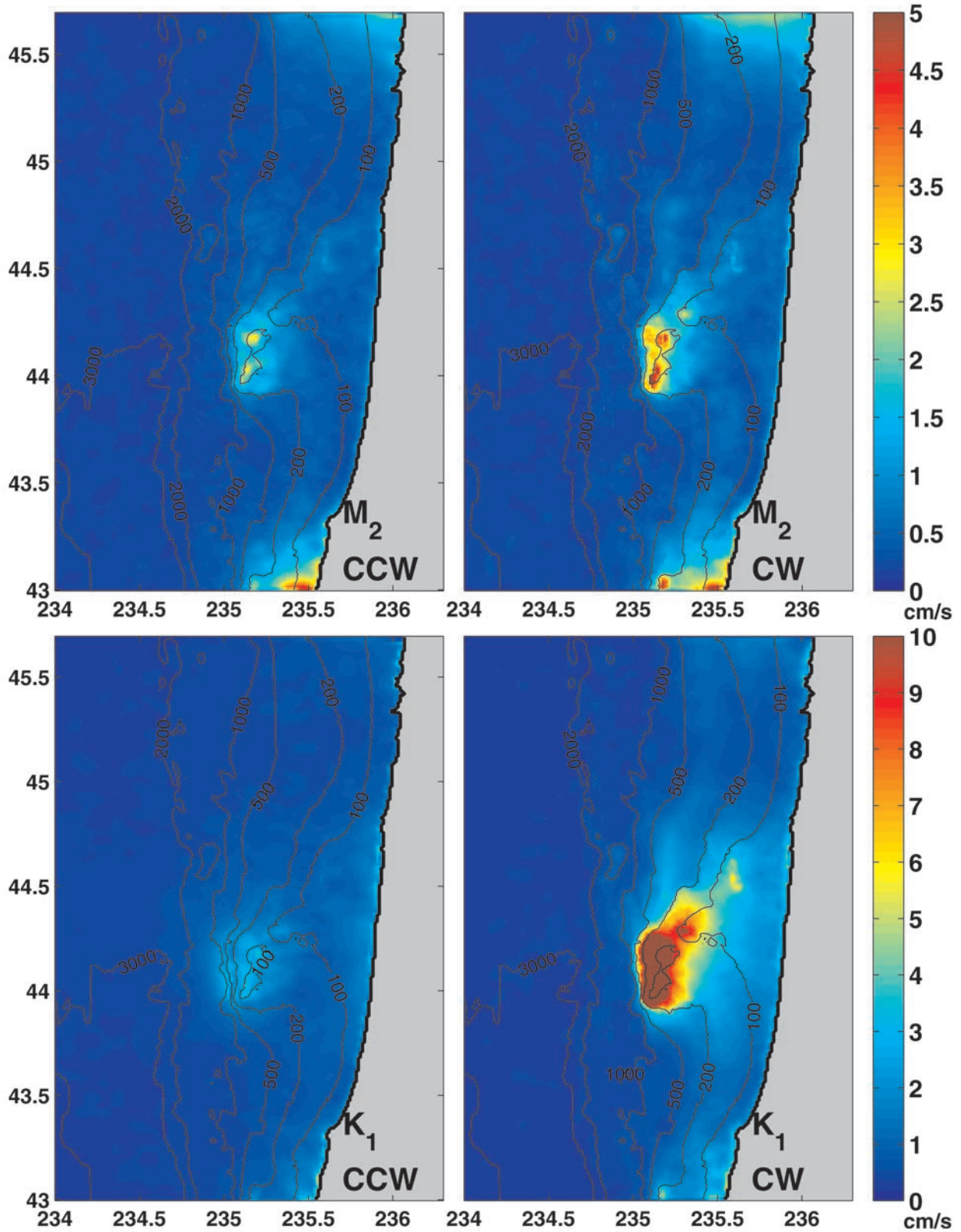


Figure 15. Posterior error standard deviation for inverse solution rotary current estimates. Note that different scales are used for M_2 and K_1 . Error amplitude peak over the HSBC and are by far largest for the K_1 CW currents.

radar data, especially in the summer when stratification is strongest on the shelf. Baroclinic currents are smallest in the winter months. Estimates of semidiurnal harmonic constants obtained from HF radar surface current data during this time period are consistent (within error bars that are less than 1 cm/s on average) with depth-averaged ADP currents and solutions to the shallow water equations. Discrepancies between observed and modeled data are consistent with plausible levels of errors in bathymetry and friction parameterizations, and in boundary conditions. Noise and contamination by baroclinic components in semidiurnal harmonic constants obtained from the HF radar surface currents are too large for these data to be useful in correcting the small errors in the modeled currents. However, comparison with the available data, including harmonic constants from a number of historical current meter moorings, suggests that our semidiurnal barotropic current model is already quite reasonable. Note that our hydrodynamic model does not explicitly include a parameterization for internal wave drag. Inclusion of this extra term, which accounts for barotropic/baroclinic energy conversion, has been shown to significantly improve tidal models at the global scale [Egbert and Ray, 2001; Jayne and St. Laurent, 2001]. The accuracy of our model without this term suggests that these processes are not energetically significant in this local domain. This conclusion is supported further by the results of Kurapov *et al.* [2003].

[66] For the subinertial diurnal band, free internal waves are not allowed, and baroclinicity on the shelf is not so evident in the HF radar or ADP data. However, diurnal tidal current harmonic constants show significant temporal variability, and stratification almost certainly plays a major role in this. A two-dimensional analysis suggests that first-mode barotropic shelf waves are permitted at the K_1 frequency over at least short sections of the Oregon coast, in particular over the HSBC in the center of the local model domain. This results in a local resonance for diurnal tidal currents in this area, and makes solutions to the shallow water equations very sensitive to details of the model configuration and forcing. Thus a priori errors in the dynamical solution are much larger for K_1 than for M_2 , and assimilation can significantly improve estimates of tidal currents in the diurnal band. The shelf wave resonance over the HSBC also appears to make the diurnal shelf currents in the ocean very sensitive to fluctuations in stratification or low-frequency background currents. Thus harmonic constants estimated from the HF radar data vary significantly over time, making definition of tidal constants for our barotropic assimilation problematic.

[67] Possibly these temporal variations in the resonant shelf wave response could be tracked by assimilation of data. However, attempts with our barotropic assimilation for summer months were not particularly successful. Comparison of summer ADP and HF radar data suggest that there is significant shear in the near surface during this time, probably due to a diurnal wind-forced component. This limits the use of the HF radar data in restoring the depth-averaged currents that we can model with the shallow water equations. A 3D stratified model, with a reasonably resolved surface boundary layer, would probably be required to assimilate summer or spring HF radar data in the diurnal band. Accounting for internal tides in the semi-

diurnal band would of course also require assimilation into a 3D model. Efforts in this direction are reported by Kurapov *et al.* [2003].

[68] By assimilation of carefully selected data, we have constructed a time-invariant harmonic model for barotropic tidal currents on the central Oregon shelf. In the process we have found that tidal currents in this area vary in a complex manner, both in space and in time. Our model may thus be of relatively limited value for actual prediction of tidal currents at any given time and location in the water column. Continuous monitoring of currents with ADP and HF radar systems would allow tracking of temporal variations in tidal constants at a few profiles, or over some area on the surface. Data assimilation with a 3D stratified model (incorporating lower frequency background currents) could in principle be used to interpolate (and extrapolate) these data to yield more reliable predictions of tidal currents throughout the coastal ocean. Such an assimilation exercise would also undoubtedly lead to further insights into the dynamics of tidal currents in the coastal ocean.

[69] **Acknowledgments.** This work was supported by grants from the National Oceans Partnership Program (N00014-98-1-0787 NOPP), the Ocean Modeling and Prediction Program (N00014-98-1-0043 ONR), and the National Science Foundation (OCE-9907854 NSF).

References

- Bennett, A. F., Inverse methods in physical oceanography, in *Monographs on Mechanics and Applied Mathematics*, 346 pp., Cambridge Univ. Press, New York, 1992.
- Bogden, P. S., The impact of model-error correlation on regional data assimilation models and their observational arrays, *J. Mar. Res.*, 59, 831–857, 2001.
- Brink, K. H., Coastal-trapped waves and wind-driven currents over the continental shelf, *Annu. Rev. Fluid Mech.*, 23, 389–412, 1991.
- Cartwright, D. E., Extraordinary tidal currents near St. Kilda, *Nature*, 223, 928–932, 1969.
- Chua, B. S., and A. F. Bennett, An inverse ocean modeling system, *Ocean Modell.* 3, pp. 137–165, Hooke Inst. Oxford Univ., Oxford, England, 2001.
- Crawford, P. F., and R. E. Thomson, Continental shelf waves of diurnal period along Vancouver Island, *J. Geophys. Res.*, 87, 9516–9522, 1982.
- Crawford, P. F., and R. E. Thomson, Diurnal period continental shelf waves along Vancouver Island: A comparison of observations with theoretical models, *J. Phys. Oceanogr.*, 14, 1629–1646, 1984.
- Cummins, P. F., D. Masson, and M. G. G. Foreman, Stratification and mean flow effects on diurnal tidal currents off Vancouver island, *J. Phys. Oceanogr.*, 30, 15–30, 2000.
- Daifuku, P. R., and R. C. Beardsley, The K_1 tide on the continental shelf from Nova Scotia to Cape Hatteras, *J. Phys. Oceanogr.*, 13, 3–17, 1983.
- Dushaw, B. D., G. D. Egbert, P. F. Worcester, B. D. Cornuelle, B. M. Howe, and K. Metzger, A TOPEX/Poseidon global tidal model (TPXO. 2) and barotropic tidal currents determined from long range acoustic transmissions, *Prog. Oceanogr.*, 40, 337–369, 1997.
- Efron, B., Nonparametric estimates of standard error: The jackknife, the bootstrap, and other resampling methods, *Biometrika*, 68, 589–599, 1981.
- Efron, B., and R. Tibshirani, Bootstrap methods for standard errors, confidence intervals, and other measures of statistical accuracy, *Stat. Sci.*, 1, 54–77, 1986.
- Egbert, G. D., Tidal data inversion: Interpolation and inference, *Prog. Oceanogr.*, 40, 81–108, 1997.
- Egbert, G. D., and A. F. Bennett, Data assimilation methods for ocean tides, in *Modern Approaches to Data Assimilation in Ocean Modeling*, edited by P. Malanotte-Rizzoli, pp. 147–179, Elsevier Sci., New York, 1996.
- Egbert, G. D., and S. Y. Erofeeva, Efficient inverse modeling of barotropic ocean tides, *J. Atmos. Oceanic Technol.*, 19, 183–204, 2002.
- Egbert, G. D., and R. D. Ray, Estimates of M_2 tidal energy dissipation from Topex/Poseidon altimeter data, *J. Geophys. Res.*, 106, 22,475–22,502, 2001.

- Egbert, G. D., A. F. Bennett, and M. G. G. Foreman, TOPEX/POSEIDON tides estimated using a global inverse model, *J. Geophys. Res.*, *99*, 24,821–24,852, 1994.
- Flather, R. A., A tidal model of the Northeast Pacific, *Atmos. Ocean*, *25*, 22–45, 1987.
- Gilbert, W. E., A. Huyer, E. D. Barton, and R. L. Smith, Physical oceanographic observations off the Oregon Coast, 1975: WISP and UP-75, *Data Rep. 64*, School of Oceanogr., Oregon State Univ., Corvallis, 1976.
- Goldfinger, C., L. D. Kulm, L. C. McNeill, and P. Watts, Super-scale failure of the southern Oregon Cascadia margin, *Pure Appl. Geophys.*, *157*, 1189–1226, 2000.
- Hendershott, M. C., The effects of solid earth deformation on global ocean tides, *Geophys. J. R. Astron. Soc.*, *29*, 389–402, 1972.
- Hendershott, M. C., Numerical models of ocean tides, in *The Sea*, edited by E. Goldberg et al., pp. 47–95, John Wiley, New York, 1977.
- Huyer, A., Seasonal variation in temperature, salinity, and density over the continental shelf off Oregon, *Limnol. Oceanogr.*, *22*, 442–453, 1977.
- International Association for Physical Sciences of the Oceans, Pelagic tidal constants, *IAPSO Pub. 35*, Woods Hole, Mass., 1992.
- Jayne, S. R., and L. C. St. Laurent, Parameterizing tidal dissipation over rough topography, *Geophys. Res. Lett.*, *28*, 811–814, 2001.
- Kosro, P. M., J. A. Austin, S. D. Pierce, J. A. Barth, M. D. Levine, T. Boyd, Time-dependent velocity structure off Newport, Oregon, during spring and summer, 1998 and 1999, paper presented at AGU Ocean Sciences Meeting, AGU, San Antonio, Tex., 2000.
- Kurapov, A. L., G. D. Egbert, R. N. Miller, and J. S. Allen, Data assimilation in a baroclinic coastal ocean model: Ensemble statistics and comparison of methods, *Mon. Weather Rev.*, *130*, 1009–1025, 2002.
- Kurapov, A. L., G. D. Egbert, J. S. Allen, R. N. Miller, S. Y. Erofeeva, and P. M. Kosro, M_2 internal tide off Oregon: Inference from data assimilation, *J. Phys. Oceanogr.*, in press, 2003.
- Lefevre, F., C. Le Provost, and F. H. Lyard, How can we improve a global ocean tide model at a regional scale? A test on the Yellow Sea and the East China Sea, *J. Geophys. Res.*, *105*, 8707–8725, 2000.
- Le Provost, C., Ocean tides, in *Satellite Altimetry and Earth Sciences*, pp. 267–303, Academic, San Diego, Calif., 2001.
- Lipa, B. J., and D. E. Barrick, Least-squares methods for the extraction of surface currents from CODAR crossed-loop data: Application at AR-SLOE, *IEEE J. Oceanic Eng.*, *8*, 226–253, 1983.
- Munk, W. H., F. Snodgrass, and M. Wimbush, Tides offshore: Transition from California coastal to deep sea waters, *Geophys. Fluid Dyn.*, *1*, 161–235, 1970.
- Pillsbury, R. D., J. S. Bottero, R. E. Still, and W. E. Gilbert, A compilation of observations from moored current meters, vol. VI, Oregon Continental Shelf, April–October 1972, *Data Rep. 57*, School of Oceanogr., Oregon State Univ., Corvallis, 1974a.
- Pillsbury, R. D., J. S. Bottero, R. E. Still, and W. E. Gilbert, A compilation of observations from moored current meters, vol. VII, Oregon Continental Shelf, July–August 1973, *Data Rep. 21*, School of Oceanogr., Oregon State Univ., Corvallis, 1974b.
- Prandle, D., Tidal currents in shelf seas—their nature and impacts, *Prog. Oceanogr.*, *40*, 245–261, 1997.
- Ray, R. D., A global ocean tide model from TOPEX/POSEIDON altimetry: GOT99. 2, *NASA/TM-1999-209478*, NASA Goddard Space Flight Center, Greenbelt, Md., 1999.
- Ray, R. D., Inversion of oceanic tidal currents from measured elevations, *J. Mar. Syst.*, *28*, 1–18, 2001.
- Rosenfeld, L. K., and R. C. Beardsley, Barotropic semidiurnal tidal currents off Northern California during the Coastal Ocean Dynamics Experiment (CODE), *J. Geophys. Res.*, *92*, 1721–1732, 1987.
- Shum, C. K., et al., Accuracy assessment of recent ocean tide models, *J. Geophys. Res.*, *102*, 25,173–25,194, 1997.
- Torgimson, G. M., and B. M. Hickey, Barotropic and baroclinic tides over the continental slope and shelf off Oregon, *J. Phys. Oceanogr.*, *9*, 945–961, 1979.
- Zelter, B. D., and W. H. Munk, The optimum wiggleness of tidal admittances, *J. Mar. Res.*, *33*, 1–13, 1975.

G. D. Egbert, S. Y. Erofeeva, and P. M. Kosro, College of Oceanic and Atmospheric Sciences, Oregon State University, 104 Ocean Admin Bldg, Corvallis, OR 97331-5503, USA. (serofeev@coas.oregonstate.edu)